

RESEARCH ARTICLE

10.1002/2017JA024772

Special Section:
Mars Aeronomy

Key Points:

- MAVEN measures the global distribution of suprathermal ions and magnetic fields around Mars, from which we can derive macroscopic forces
- The flows, fields, and forces in the Mars-solar wind interaction vary with both upstream magnetic field orientation and Mach number
- Ion temperature and temperature anisotropy vary spatially and with solar wind parameters, with implications for plasma instabilities

Correspondence to:

J. S. Halekas,
jasper-halekas@uiowa.edu

Citation:

Halekas, J. S., Brain, D. A., Luhmann, J. G., DiBraccio, G. A., Ruhunusiri, S., Harada, Y., ... Jakosky, B. M. (2017). Flows, fields, and forces in the Mars-solar wind interaction. *Journal of Geophysical Research: Space Physics*, 122. <https://doi.org/10.1002/2017JA024772>

Received 11 SEP 2017

Accepted 4 NOV 2017

Accepted article online 8 NOV 2017

Flows, Fields, and Forces in the Mars-Solar Wind Interaction

J. S. Halekas¹ , D. A. Brain², J. G. Luhmann³ , G. A. DiBraccio⁴, S. Ruhunusiri¹ , Y. Harada¹ , C. M. Fowler², D. L. Mitchell³ , J. E. P. Connerney⁴, J. R. Espley⁴, C. Mazelle⁵ , and B. M. Jakosky² ¹Department of Physics and Astronomy, University of Iowa, Iowa City, IA, USA, ²Laboratory for Atmospheric and Space Physics, University of Colorado Boulder, Boulder, CO, USA, ³Space Sciences Laboratory, University of California, Berkeley, CA, USA, ⁴NASA Goddard Space Flight Center, Greenbelt, MD, USA, ⁵IRAP, University of Toulouse, CNRS, UPS, CNES, Toulouse, France

Abstract We utilize suprathermal ion and magnetic field measurements from the Mars Atmosphere and Volatile Evolution (MAVEN) mission, organized by the upstream magnetic field, to investigate the morphology and variability of flows, fields, and forces in the Mars-solar wind interaction. We employ a combination of case studies and statistical investigations to characterize the interaction in both quasi-parallel and quasi-perpendicular regions and under high and low solar wind Mach number conditions. For the first time, we include a detailed investigation of suprathermal ion temperature and anisotropy. We find that the observed magnetic fields and suprathermal ion moments in the magnetosheath, bow shock, and upstream regions have observable asymmetries controlled by the interplanetary magnetic field, with particularly large asymmetries found in the ion parallel temperature and anisotropy. The greatest temperature anisotropies occur in quasi-perpendicular regions of the magnetosheath and under low Mach number conditions. These results have implications for the growth and evolution of wave-particle instabilities and their role in energy transport and dissipation. We utilize the measured parameters to estimate the average ion pressure gradient, $J \times B$, and $v \times B$ macroscopic force terms. The pressure gradient force maintains nearly cylindrical symmetry, while the $J \times B$ force has larger asymmetries and varies in magnitude in comparison to the pressure gradient force. The $v \times B$ force felt by newly produced planetary ions exceeds the other forces in magnitude in the magnetosheath and upstream regions for all solar wind conditions.

Plain Language Summary The solar wind that flows out from the Sun and pervades our solar system is largely deflected around Mars by its interaction with the upper atmosphere. However, this interaction also transfers energy to planetary ions, giving some of them sufficient velocity to escape from Mars. Therefore, the Mars-solar wind interaction has implications for the long-term evolution of the Martian atmosphere and its habitability. In this work, we study the structure and variability of the interaction and the macroscopic forces responsible for decelerating and deflecting the solar wind around Mars as well as those that accelerate planetary ions. We also investigate the asymmetries in this interaction and how they change in response to variations in the incoming solar wind flow and the magnetic field carried with the flow.

1. Introduction

Despite fundamental physical differences, most notably the lack of an intrinsic global planetary magnetic field, the Mars-solar wind interaction has many features in common with that at the Earth. Like Earth, Mars has a bow shock, an upstream foreshock, a magnetosheath, and an inner magnetosphere and magnetotail, as reviewed by many authors (Bertucci et al., 2011; Dubinin et al., 2006; Mazelle et al., 2004; Nagy et al., 2004). The Martian magnetosphere is dominated by plasma of atmospheric origin, which forms the primary global obstacle to the solar wind through induction and mass loading, with additional contributions from localized crustal magnetic fields. This stands in contrast to the terrestrial case, where the intrinsic magnetic field provides the primary obstacle to the solar wind flow. Nonetheless, at both planets, a bow shock and magnetosheath form to decelerate and deflect the solar wind flow around the magnetosphere.

However, although the bow shock and the magnetosheath play similar roles at Mars, Earth, and other planets throughout the solar system, Mars' small size leads to some critical differences. Whereas at Earth and Venus, the bow shock and magnetosheath have scales much larger than solar wind ion scales, at Mars, the magnetosheath has a thickness on the order of the convected ion gyroradius and a lateral scale only an order of

magnitude greater. Moses, Coroniti, and Scarf (1988) recognized that the small scale of the Martian magnetosheath implied that the solar wind likely could not fully thermalize before encountering the obstacle for typical solar wind conditions, suggesting a more kinetic interaction in which shocked solar wind could directly affect the magnetosphere and ionosphere.

In addition to its small size, the Martian magnetosheath has other complicating factors not present at Earth. Both heavy ions (Dubinin et al., 1997) and cold protons (Dubinin et al., 1993) of exospheric origin can originate in and/or access the upstream region, bow shock, and magnetosheath, potentially affecting the structure of the interaction. These planetary ions can affect the interaction in an asymmetric manner thanks to their gyration, which can have large scales compared to the interaction, particularly for heavy species. Crustal magnetic fields further perturb the bow shock and magnetosheath structure (Brain et al., 2005; Dong et al., 2015; Edberg et al., 2009; Fang et al., 2017; Luhmann et al., 2002; Ma et al., 2014; Mazelle et al., 2004). Nonetheless, despite these various sources of complexity, the basic morphology of the observed bulk flows and fields at Mars corresponds at least approximately to predictions from relatively simple gas-dynamic models (Crider et al., 2004; Kallio et al., 1994).

The scientific investigation of the Mars-solar wind interaction began with Mariner-4 and the early Soviet Mars missions and continued with Phobos-2, Mars Global Surveyor (MGS), and Mars Express (MEX). The Mars-2, 3, and 5 missions measured solar wind deceleration, deflection, and heating indicative of the presence of a bow shock and magnetosheath (Vaisberg, 1992). Phobos-2 revealed more details of the interaction, including interplanetary magnetic field (IMF)-controlled asymmetry of the shock and magnetosheath (Dubinin et al., 1998), and a high level of wave activity in the upstream region and magnetosheath (Russell et al., 1990; Sagdeev et al., 1990). MGS added further detail to our understanding of the kinetic physics of the magnetosheath, returning measurements indicating a high occurrence of linearly polarized low-frequency waves, possibly resulting from mirror mode instabilities (Bertucci et al., 2004; Espley et al., 2004). MEX filled in still more details, comprehensively mapping the ion flow around Mars (Fraenz et al., 2006) and elucidating how thermal pressure in the magnetosheath balances solar wind dynamic pressure on the upstream side and magnetic pressure from the piled up field on the downstream side (Dubinin et al., 2008).

Now the Mars Atmosphere and Volatile Evolution (MAVEN) mission (Jakosky et al., 2015) provides the first simultaneous in situ magnetic field and ion flux measurements since Phobos-2, from an elliptical orbit that offers comprehensive coverage of the magnetosphere over a wide range of solar zenith angles, local times, solar latitudes, geographic locations, solar wind conditions, and seasons. MAVEN's observations have already contributed to our understanding of the distribution and variability of electromagnetic waves around Mars, indicating a high occurrence rate of waves at the proton cyclotron frequency upstream from the bow shock (Romanelli et al., 2016), Alfvén waves in both the upstream region and magnetosheath and fast mode waves near the bow shock (Ruhunusiri et al., 2015), the prevalence of wave power in multiple frequency bands throughout the magnetosheath (Fowler et al., 2017), and heating and dissipation in the magnetosheath but an apparent absence of fully developed turbulence (Ruhunusiri et al., 2017). All of these results indicate the presence of nonthermal distribution functions and associated plasma instabilities, reinforcing the idea that the small size of the Martian magnetosheath may not allow full thermalization of the incident solar wind protons for typical conditions, as suggested by Moses et al. (1988).

In this manuscript, we now utilize MAVEN's unique capabilities to investigate the macroscopic flows, fields, and forces in the Mars-solar wind interaction, to map out their average characteristics, and to understand how they vary as a function of solar wind and IMF conditions.

2. MAVEN Observations

We utilize measurements from the Solar Wind Ion Analyzer (SWIA) (Halekas et al., 2015, 2017) and Magnetometer (MAG) (Connerney, Espley, Lawton, et al., 2015; Connerney, Espley, DiBraccio, et al., 2015) for both case studies and statistical investigations, together with supporting observations from the Solar Wind Electron Analyzer (SWEA) (Mitchell et al., 2016) for case studies. We use only fully calibrated Level 2 observations. As described by Halekas et al. (2017), the SWIA instrument returns several different types of data, including two different types of 3-D velocity distributions and onboard-computed moments and energy spectra. In this work, we utilize both "fine" distributions that cover a limited range of phase space with high

resolution and “coarse” distributions that cover the full SWIA angular and energy range with lower resolution. We exclusively utilize 3-D distributions and moments and spectra derived from them rather than relying on onboard-computed quantities.

Since the MAVEN spacecraft does not spin, its particle instruments cannot provide complete angular coverage. The SWIA instrument utilizes electrostatic deflection to provide up to $360^\circ \times 90^\circ$ coverage (with some obstructions, less for energies >4.5 keV). For nominal spacecraft orientations, SWIA’s accommodation provides optimal coverage of the solar wind and magnetosheath flow (Halekas et al., 2015); however, portions of the distribution in the magnetosheath can still fall outside the field of view (FOV), especially in the subsolar region where the incident flow experiences the greatest deceleration and deflection. Though the FOV extends to cover sunward going particles, reflected populations (as well as pickup ions) can also fall into the holes in the FOV. Therefore, though SWIA typically covers the majority of the distribution, its measurements technically can only provide a lower limit on the total ion density. SWIA’s incomplete FOV can also result in errors in other derived ion moments such as bulk flow velocity and temperature. Given a narrow supersonic distribution (such as the solar wind) with its center contained in the FOV, SWIA can obtain good measurements of both bulk flow and temperature; however, for a broader subsonic or transonic distribution, SWIA can typically only resolve two of the three components of the temperature, since a cut across the distribution along at least one axis will fall into the holes in the FOV.

In addition to FOV issues, the presence of heavy ions complicates the interpretation of velocity distributions from SWIA (which does not measure ion composition), as described by Halekas et al. (2017). Solar wind scattering from spacecraft and instrument surfaces also contributes a background small in magnitude but nonetheless capable of affecting ion temperature estimates, largely due to its widespread angular distribution (Halekas et al., 2017). In order to overcome these issues, in this work we concentrate primarily on measurements made in the upstream region and magnetosheath, where protons represent the dominant species. Within the ionosphere and magnetosphere we do not attempt to utilize the SWIA measurements for quantitative purposes, since heavy planetary ions dominate these environments and a large portion of the ion distribution lies below the energy range of the SWIA measurement. Elsewhere, we take measures (described below) to minimize the effects of scattered solar wind and to select only observations that best represent the full proton velocity distribution.

We utilize magnetic field measurements from MAG (Connerney, Espley, Lawton, et al., 2015; Connerney, Espley, DiBraccio, et al., 2015) to organize our observations. We use fully corrected level 2 data averaged to 1 s resolution throughout and sampled at the times of the charged particle measurements as appropriate to produce distribution functions in magnetic field-aligned coordinates. Finally, we utilize SWEA observations for context. SWEA provides electron differential energy fluxes over a $360^\circ \times 120^\circ$ range (with some obstructions), providing nearly complete sampling of electron velocity distributions.

Figures 1–3 display MAVEN SWEA, MAG, and SWIA observations for three orbits selected from a 1 week period in January 2017. All three orbits have essentially the same geometry, with the inbound bow shock crossing near the flank (just sunward of the terminator), the outbound bow shock crossing at a solar zenith angle (SZA) of $\sim 45^\circ$, and periapsis on the nightside. We compute the angle θ_{bn} between the magnetic field and the bow shock normal assuming a conical bow shock surface (Edberg et al., 2008, 2009, 2010; Halekas et al., 2017; Trotignon et al., 2006). We compute the Alfvén Mach number from the magnetic field magnitude, ion density, and ion flow speed averaged over the upstream interval as described in section 3.1 of Halekas et al. (2017). Both bow shock crossings for the orbit in Figure 1 have quasi-perpendicular geometry, and the solar wind has a high Alfvén Mach number. The orbit in Figure 2 also occurs under high Mach number conditions but has a quasi-parallel outbound shock crossing. Finally, the orbit in Figure 3 also has quasi-perpendicular shock crossings but occurs under low Mach number conditions.

We estimate the density, velocity, pressure, and temperature moments by computing weighted sums over the measured coarse 3-D ion velocity distributions measured by SWIA, which cover energies of 25–25,000 eV with binned energy resolution of $\sim 15\%$ and the full angular range with a resolution of $22.5^\circ \times 22.5^\circ$. For times when the SWIA instrument was in “solar wind mode” we also display proton core temperatures derived from fine 3-D ion velocity distributions (with the solar wind alpha particle population removed by windowing in energy per charge (Halekas et al., 2017)), which cover a portion of the distribution around the peak with binned energy resolution of 7.5% and angular resolution of $3.75^\circ \times 4.5^\circ$. We calculate the pressure tensor

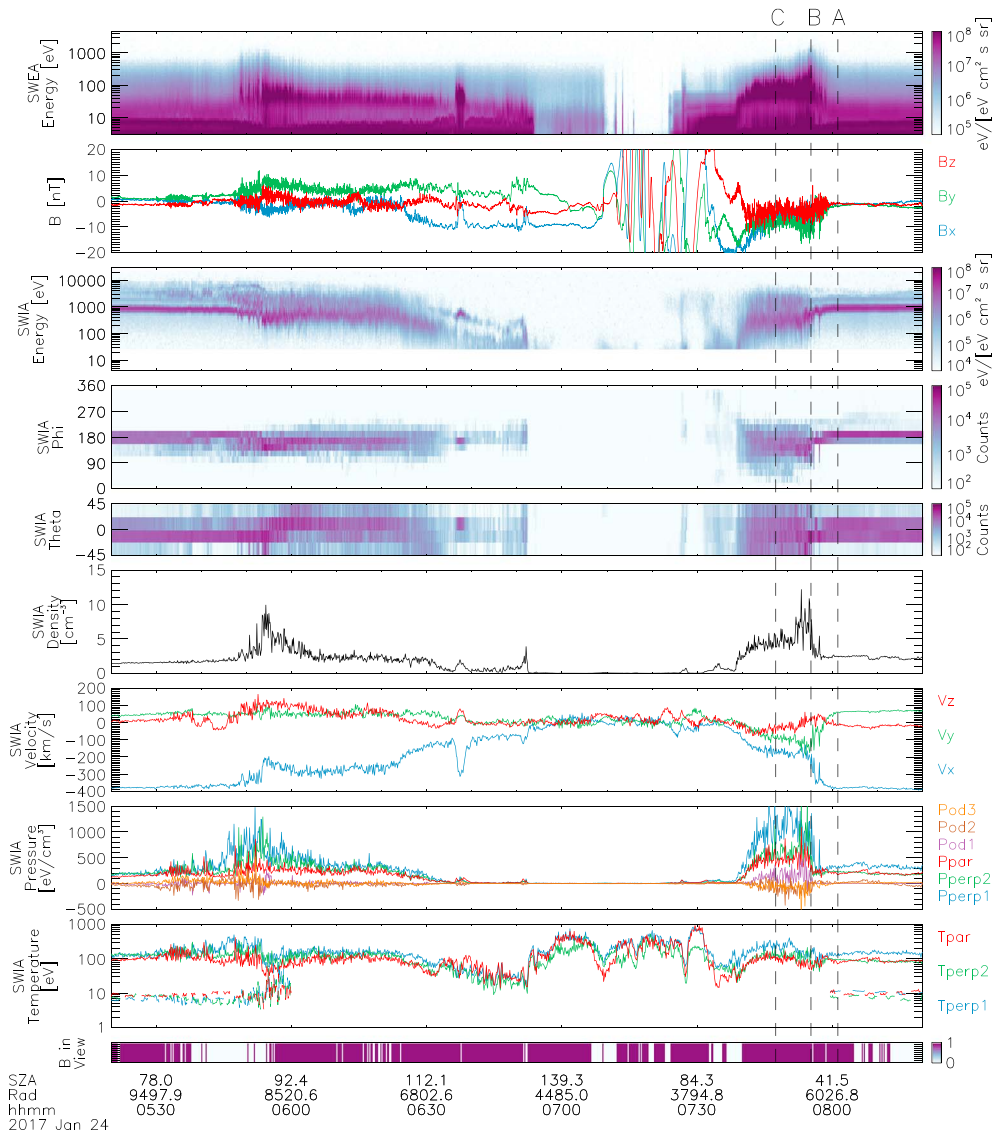


Figure 1. MAVEN observations from an orbit with quasi-perpendicular inbound ($\theta_{Bn} \sim 84^\circ$) and outbound ($\theta_{Bn} \sim 78^\circ$) shock crossings and solar wind Alfvén Mach numbers of ~ 10 inbound and ~ 22 outbound. From top to bottom, the panels show electron energy spectra, magnetic field in Mars-Solar-Orbital (MSO) coordinates, ion energy and angular spectra in instrument coordinates, ion density, ion velocity in MSO coordinates, and ion pressure and temperature in magnetic field-aligned coordinates. The color bar indicates times with the magnetic field vector within the SWIA FOV. All ion measurements are derived from SWIA coarse 3-D distributions, except for the core proton temperature derived from fine 3-D distributions (dashed lines). “A,” “B,” and “C” indicate the observation times of velocity distributions displayed in Figure 4.

in instrumental coordinates and then rotate it into magnetic field-aligned coordinates by first aligning one axis with the magnetic field to obtain the parallel pressure (P_{par}) and then diagonalizing the two perpendicular components (P_{perp1} and P_{perp2}). For a well-formed diagonal pressure tensor, our computation will return $P_{perp1} \geq P_{perp2}$. We compute the corresponding temperature components by dividing the diagonal pressure tensor elements by the density. Physically, the off-diagonal elements of the pressure tensor (P_{od1} , P_{od2} , and P_{od3}) represent shear viscosity, which we expect to be small. Nonzero off-diagonal elements therefore likely at least in part represent the uncertainty of the pressure tensor measurement.

Note that a gyrotropic distribution has equal perpendicular pressure components ($P_{perp1} = P_{perp2}$). However, we do not expect gyrotropy to hold near discontinuities such as the bow shock, or even in the

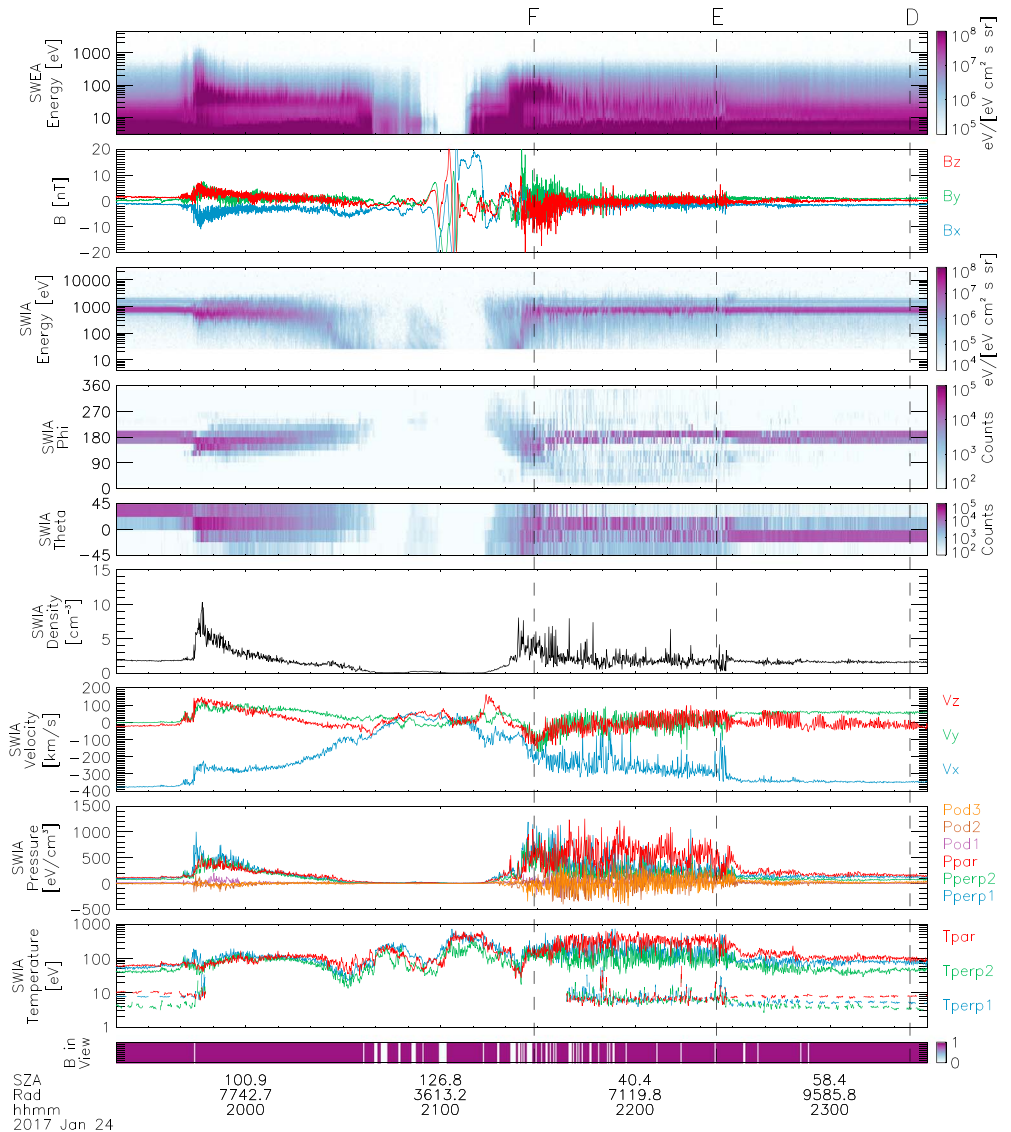


Figure 2. MAVEN observations from an orbit with quasi-perpendicular inbound ($\theta_{Bn} \sim 87^\circ$) and quasi-parallel outbound ($\theta_{Bn} \sim 159^\circ$) shock crossings and Alfvén Mach numbers of ~ 13 inbound and ~ 12 outbound. All panels same as Figure 1. “D,” “E,” and “F” indicate the observation times of velocity distributions displayed in Figure 4.

magnetosheath, given its small scale. Furthermore, even given perfect gyrotropy, the incomplete FOV described above will typically lead to differences in the measured perpendicular pressure components. Since we wish to characterize pressure and temperature anisotropies in the following sections, we will select times with the magnetic field direction within the $360^\circ \times 90^\circ$ nominal SWIA FOV for further analysis. At these times, we can obtain good measurements of the parallel pressure and at least one of the perpendicular components. Since we expect the well-measured perpendicular component to be larger than the poorly measured one, we take the principal perpendicular component P_{perp1} as our best estimate of the perpendicular pressure (technically, an upper limit to the perpendicular pressure, since we pick the maximum eigenvalue), and likewise for the corresponding temperature component, which we identify as $T_{\text{perp1}} = T_{\text{perp_max}}$.

The observations in Figures 1–3 display the wide range of variability in the Mars-solar wind interaction. Despite identical orbit geometries, the extent and morphology of the foreshock, shock, and magnetosheath vary dramatically, as a result of the changes in IMF direction and solar wind parameters. In all cases, we can identify the magnetosheath by the combination of the enhanced suprathermal electron population (with

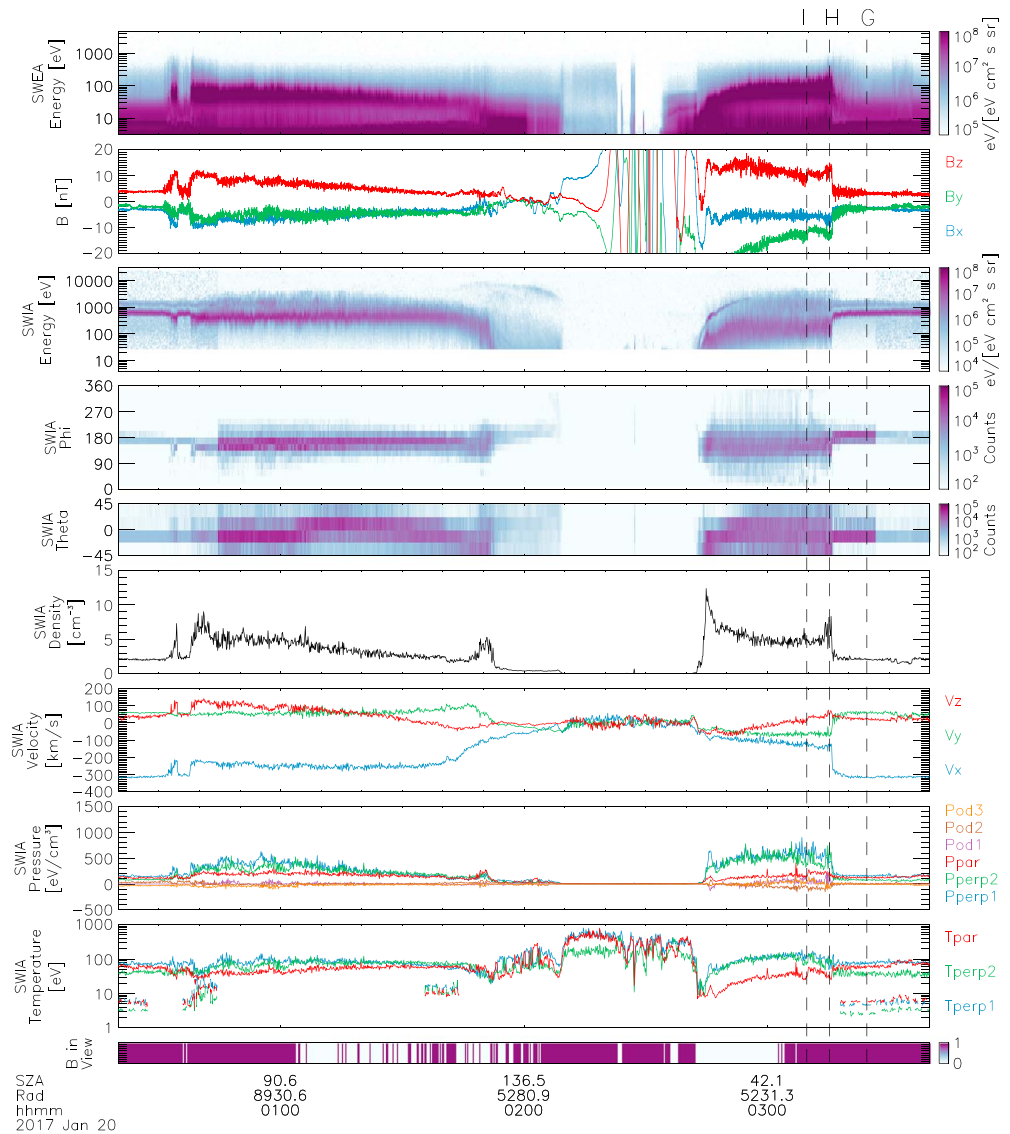


Figure 3. MAVEN observations from an orbit with quasi-perpendicular inbound ($\theta_{Bn} \sim 85^\circ$) and outbound ($\theta_{Bn} \sim 98^\circ$) shock crossings and Alfvén Mach numbers of ~ 4.2 inbound and ~ 4.3 outbound. All panels same as Figure 1. Changes in SWIA count rate at 01:45 and 03:26 result from the mechanical attenuator opening/closing. “G,” “H,” and “I” indicate the observation times of velocity distributions displayed in Figure 4.

maximum flux at ~ 50 – 100 eV) and the high level of low-frequency fluctuations in the magnetic field. We can generally also observe deflection, deceleration, compression, and heating of the ion population in the magnetosheath, but these signatures vary widely with upstream conditions.

In all cases we observe an increase in the total suprathermal ion pressure in the magnetosheath, as required to balance the reduction in dynamic pressure across the shock, typically with a larger increase on the more subsolar outbound crossings where the normal component of the dynamic pressure must experience a larger reduction. However, for the quasi-perpendicular shock crossings, we find a greater increase in the perpendicular pressure (particularly near the bow shock), while for the quasi-parallel case of Figure 2, we instead observe a larger parallel pressure increase. For all quasi-perpendicular crossings we observe a peak in density at the bow shock and a decrease within, but the magnitude and extent of this overshoot vary. For the quasi-parallel case, it proves difficult to even identify a clear bow shock, and disturbances to the magnetic field and ion distribution reach well upstream in an extended foreshock region, much as in the terrestrial quasi-parallel

shock (Schwartz & Burgess, 1991). Meanwhile, for the low Mach number orbit of Figure 3, the shock and magnetosheath display a smaller increase in density and a smoother profile in both the ion moments and the magnetic field. This smoother behavior suggests a lower level of low-frequency wave activity, as expected given the reduced ion reflection typical for low Mach number shocks (Hada et al., 2003).

In the region upstream from the bow shock, the SWIA coarse measurements do not resolve the ion distribution, and they contain contributions from both alpha particles and scattered solar wind, as well as pickup ions from the hydrogen and oxygen coroneae. Therefore, the pressure and temperature moments derived from coarse distributions in the solar wind should be regarded as only an upper limit. The core temperature measurements computed from fine distributions indicate solar wind temperatures much lower than those downstream from the bow shock, as expected.

The ion temperature increase we observe in the magnetosheath likely results from a combination of multiple effects. First, the distribution experiences heating as a result of the compression of the plasma across the shock. We can approximately describe this heating utilizing the Chew-Goldberger-Low (CGL) (Chew et al., 1956) or “double-adiabatic” equations, which predict $\frac{T_{\perp}}{B} = \text{constant}$, $\frac{T_{\parallel} B^2}{\rho^2} = \text{constant}$. Together, these equations predict a temperature anisotropy of the form $\frac{T_{\perp}}{T_{\parallel}} = \left(\frac{\rho_0}{\rho}\right)^2 \left(\frac{B}{B_0}\right)^3$ for an initially isotropic distribution experiencing compression along a streamline (Crooker & Siscoe, 1977). For a quasi-parallel planar shock the CGL equations predict greater parallel heating (given the smaller magnetic field amplification expected for this geometry), while for a quasi-perpendicular shock they predict greater perpendicular heating. This prediction proves consistent with the MAVEN observations shown in Figures 1–3, despite the fact that the CGL assumptions (for instance, Maxwellian distributions) do not always hold at Mars.

The compression effect can produce ion distributions with very high anisotropy in the magnetosheath, which can drive instabilities such as mirror and ion cyclotron modes (Gary et al., 1993) that can further modify the distribution. Observations at the Earth suggest that such instabilities can effectively transfer energy between perpendicular and parallel temperature components, thereby limiting the magnitude of the anisotropy that can develop (Hill et al., 1995).

At supercritical shocks such as those shown in Figures 1–3 (and occurring the vast majority of the time at Mars), ion reflection plays an important role in the dissipation, and reflected ions populate the region near the shock as well as the downstream magnetosheath (Paschmann et al., 1982; Scokpe et al., 1983, 1990). At quasi-parallel shocks, these reflected ions can travel large distances into the upstream region (Gosling et al., 1982), contributing to the extended nature of the quasi-parallel interaction. The presence of these reflected ions, with velocities distinct from the solar wind, necessarily leads to an increase in the measured suprathermal ion pressure and temperature not explicitly captured by the compression effect described above.

In Figure 4, we show sample distributions from the orbits of Figures 1–3, taken from approximately comparable locations in the magnetosheath and upstream region on the outbound segment. The three orbits differ mainly in the orientation and strength of the IMF (with the latter primarily responsible for the differences in Mach number). On the other hand, the upstream solar wind has relatively comparable moments, with proton densities of 1.5–2.3 cm⁻³, proton flow speeds of 340–410 km/s, proton temperatures of 5–10 eV with at most minor thermal anisotropies, and 2–3% alpha particle content (all values estimated from the fine distributions in Figures 4a, 4d, and 4g using two-component moment computations (Halekas et al., 2017)).

However, just inside the shock, SWIA coarse measurements (Figures 4b, 4e, and 4h) reveal dramatic differences in the modified ion distributions. All three have observable reflected ion populations, but for the quasi-perpendicular cases (Figures 4b and 4h) these are separated from the main incident population mostly in the perpendicular direction, whereas in the quasi-parallel case (Figure 4e) the separation is in the parallel direction, consistent with quasi-specular reflection from the bow shock and/or magnetic barrier. Regardless of the mechanism, all three distributions display large departures from a Maxwellian distribution. The combination of heating of the core and the addition of reflected ions increases the effective measured temperature by a factor of ~10–15 with respect to the solar wind core in the quasi-perpendicular cases, and a factor of ~30 in the quasi-parallel case. The quasi-perpendicular cases both have thermal anisotropies $\left(\frac{T_{\perp}}{T_{\parallel}}\right)$ of ~2.7, while the quasi-parallel case has an anisotropy of ~0.3. Compared to the upstream value, the bulk ion velocity is ~40% lower in the quasi-perpendicular high Mach number case (Figure 4b), ~20% lower in

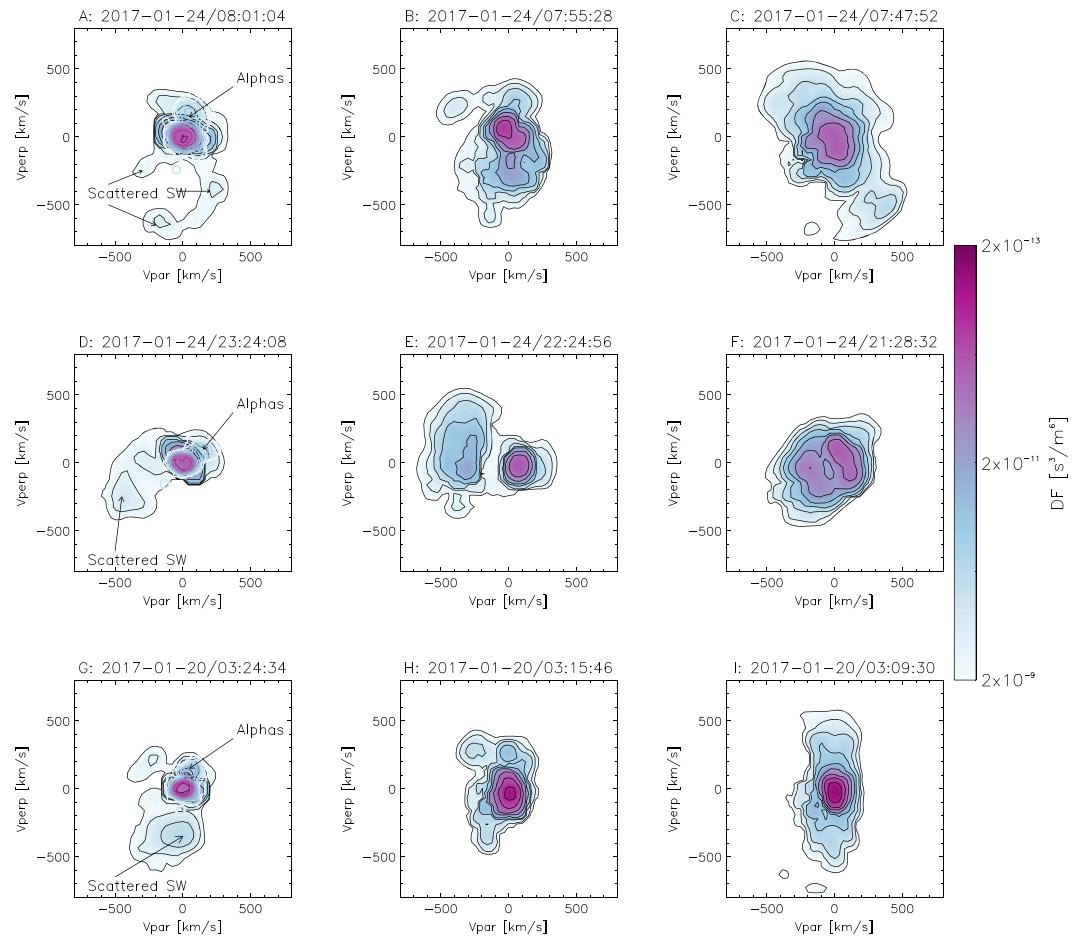


Figure 4. Ion velocity distributions measured by SWIA on the orbits shown in Figures 1–3, in magnetic field-aligned coordinates. Each panel shows a cut through the measured 3-D distribution in the plane containing the magnetic field and bulk ion velocity, in the plasma frame defined by the ion velocity. (a, d, and g) Distributions measured in the upstream region, with unfilled contours showing fine velocity distributions and filled contours representing coarse distributions. (b, e, and h) Coarse distributions just inside the bow shock. (c, f, and i) Coarse distributions in the central magnetosheath. The arrows in Figures 4a, 4d, and 4g identify protons scattered from instrumental surfaces and solar wind alphas.

the quasi-parallel case (Figure 4e), and $\sim 60\%$ lower in the low Mach number case (Figure 4h). Both quasi-perpendicular cases have density amplifications of a factor of ~ 2.5 , whereas in the quasi-parallel case the density barely increases.

Deeper in the magnetosheath, the observed distributions evolve to more closely approach a Maxwellian form. However, in the high Mach number cases (Figures 4c and 4f) observable non-Maxwellian features still clearly exist. Compared to the upstream solar wind core temperature, both quasi-perpendicular cases (Figures 4c and 4i) have temperature amplifications of ~ 15 , while the quasi-parallel case (Figure 4f) has a temperature amplification of ~ 30 , all similar to the values observed just inside the shock. The high Mach number magnetosheath distributions have anisotropies of ~ 2.2 for the quasi-perpendicular case (Figure 4c) and ~ 1.1 for the quasi-parallel case (Figure 4f), both less extreme than observed just inside the shock. This reduction in anisotropy likely indicates the effect of wave-particle interactions that have acted to reduce anisotropy across the magnetosheath. On the other hand, in the low Mach number case (Figure 4i), the anisotropy increases to ~ 4.0 , and this distribution approaches a bi-Maxwellian form. The higher anisotropy may result from the higher thresholds for ion cyclotron and mirror mode instabilities for low values of ion β (the ratio of ion thermal pressure to magnetic pressure) expected for low upstream Mach numbers. Compared to the upstream value, the bulk ion velocity is $\sim 60\%$ lower in the quasi-perpendicular high Mach number case (Figure 4c), $\sim 40\%$ lower in the quasi-parallel case (Figure 4f), and $\sim 70\%$ lower in the low Mach

number case (Figure 4i). In all cases we find a lower flow speed, but not drastically reduced compared to that observed just inside the shock. The density has a slightly larger value than that measured just inside the shock for the quasi-parallel case, but a slightly lower value for the quasi-perpendicular cases. The magnetic field magnitude displays a similar trend.

Though the sense of the thermal anisotropy measured in our three case studies matches that expected from the double adiabatic theory, it appears that reflected ion populations have an important and even dominant influence on the measured temperatures and anisotropies, particularly near the bow shock. The evolution of the observed anisotropy across the magnetosheath also does not obviously correspond to the CGL predictions, which should not surprise us greatly, given the highly non-Maxwellian distributions we observe. The measured anisotropies, particularly close to the shock, exceed the average anisotropies observed in the terrestrial magnetosheath (Dimmock et al., 2015); however, they compare favorably to those observed downstream from low Mach number shocks and very close to high Mach number shocks (Sckopke et al., 1990). Given the much smaller scale of the Martian magnetosheath, these values appear reasonable.

The time series in Figures 1–3 show that large-amplitude fluctuations in all quantities persist throughout the bow shock and magnetosheath, particularly in the high Mach number cases. Therefore, we can hardly consider the values measured for three sample distributions per orbit generally representative. To obtain a more meaningful representation of the average interaction, we will utilize the large number of MAVEN orbits to construct statistical distributions. These necessarily average over many of the observed fluctuations but help provide a sense of the typical equilibrium behavior of the Mars-solar wind interaction.

3. Average Properties of the Mars-Solar Wind Interaction

In order to better understand the Mars-solar wind interaction, we now investigate a statistical compilation of observations spanning the time period from the beginning of the MAVEN mission in 6 October 2014 through 11 June 2017, covering more than one Martian year from a variety of observational viewpoints and under a wide variety of solar wind conditions. We filter all SWIA coarse distributions and corresponding magnetic field observations from MAG to select those from time periods for which MAVEN also measured the upstream solar wind and IMF (as identified using the algorithm of Halekas et al., 2017) on the same orbit, and we further select only observations for which the instantaneously measured magnetic field lay within the SWIA FOV, in order to enable reliable estimation of both parallel and perpendicular pressure and temperature components. We do not apply any criteria requiring the peak of the distribution to lie within the SWIA FOV. For the vast majority of the time the nominal Sun-pointing orientation of the spacecraft ensures good coverage of the distribution in the magnetosheath and upstream region; however, within the magnetosphere this does not necessarily hold true.

After selecting all observations that meet the criteria defined above, we use the average IMF measured in the corresponding upstream solar wind interval to rotate observations from each orbit into Mars-Solar-Electric (MSE) coordinates, aligned so that the IMF lies in the x - y plane with a positive y component, and the $+x$ axis points sunward. We do not correct for the aberration due to the orbital motion of Mars around the Sun, since for typical conditions the aberration angle is only $\sim 5^\circ$, comparable to the resolution of the SWIA coarse distributions. After transforming coordinate frames for each orbit, and normalizing most quantities by their upstream values, we bin all observations into a 3-D grid, with 500 km resolution in the x - y plane, and 2000 km resolution in the z direction. This coarse grid cannot resolve the low-altitude interaction but suffices to investigate the magnetosheath and upstream regions. Note that one can only interpret the suprathermal ion parameters in a quantitative fashion in the upstream and magnetosheath. At lower altitudes in the magnetic pileup region, ionosphere, and magnetotail, the dominant presence of heavy ions and the existence of populations outside of the measured energy range and FOV imply that we can at best interpret the ion moments in a qualitative fashion in those regions. The magnetic field measurements have no such limitations.

The results, shown in Figure 5, largely conform to expectations based on previous measurements and simulations. The density and flow patterns largely reproduce those derived from MEX observations (Fraenz et al., 2006) and those previously derived from MAVEN observations (Halekas et al., 2017), while the magnetic field draping pattern essentially reproduces that previously derived from MGS (Crider et al., 2004) and MAVEN (Connerney, Espley, DiBraccio, et al., 2015) observations. The observed morphology of the fields and flows

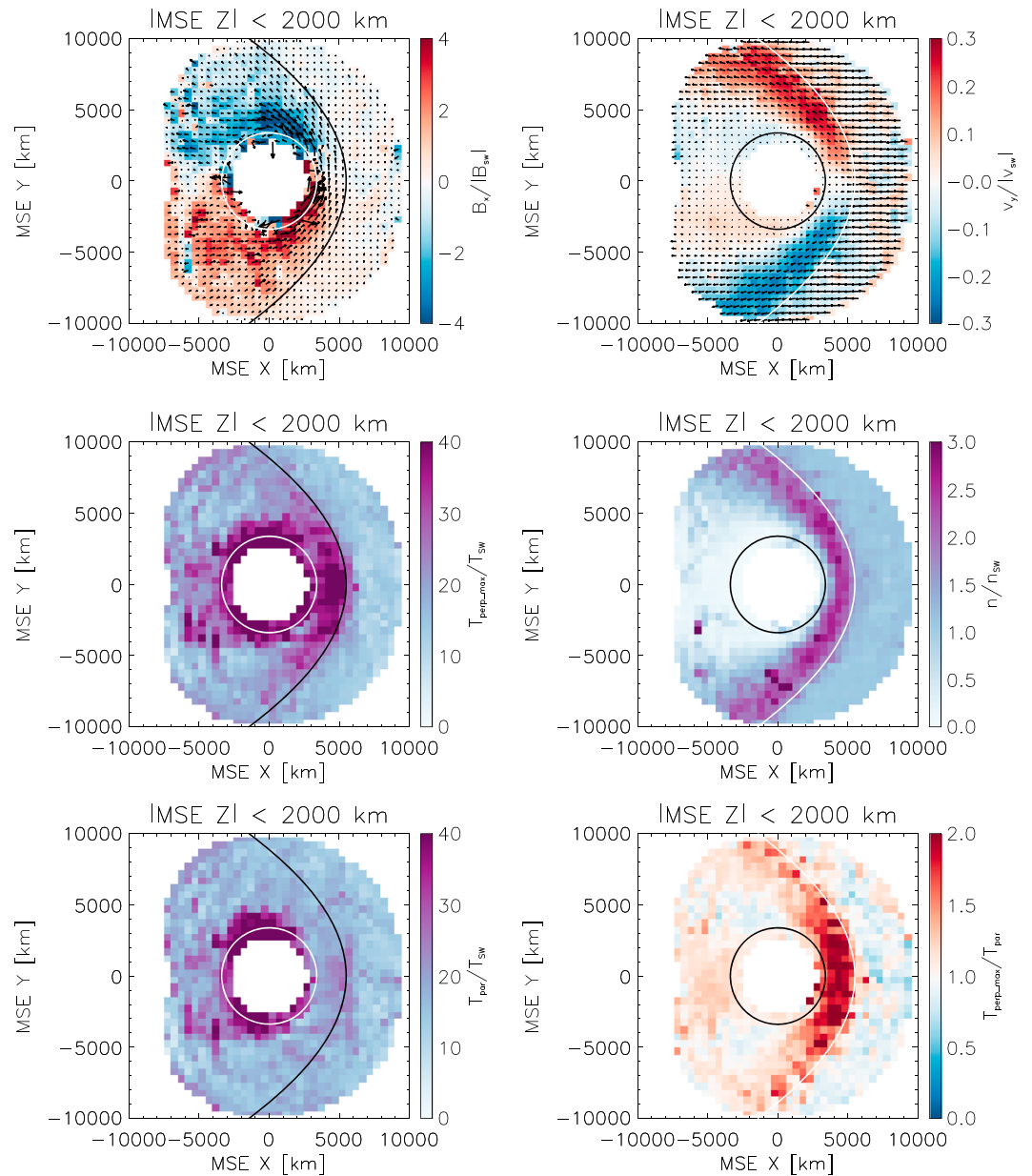


Figure 5. Average magnetic field component B_{xi} , suprathermal ion velocity component V_{yi} , suprathermal ion density, and suprathermal ion temperature components and anisotropy, in the MSE x - y plane. All quantities except anisotropy are normalized by upstream values before averaging. The arrows in the magnetic field and ion flow panels indicate normalized vector components in the x - y plane. The curves in each panel show the Martian radius and the nominal bow shock location from Trotignon et al. (2006).

also matches that expected from MHD and hybrid models of the induced magnetospheric interaction at Mars (Boesswetter et al., 2004; Brain et al., 2010; Brecht & Ledvina, 2007; Dong et al., 2014; Ma et al., 2004; Modolo et al., 2006, 2016; Najib et al., 2011), with the characteristic compression, deceleration, and deflection in the magnetosheath accompanied by magnetic field draping and pileup around the obstacle. Since we average over all subsolar longitudes and rotate into MSE coordinates, we cannot distinguish most of the effects of crustal magnetic fields, which depend on the rotational phase and geographic orientation of Mars.

For the first time, we obtain an estimate of the global morphology of the ion temperature components and anisotropy around Mars. We find a region of enhanced perpendicular ion temperatures extending throughout the magnetosheath, with the highest temperatures observed near the bow shock, particularly in the

subsolar region. This result conforms to expectations based on the compression across the shock and the addition of reflected ions, as discussed above. On the other hand, the parallel temperature shows only a very small increase, at least in an average sense (note that the results shown in Figure 5 average over all IMF directions and include both quasi-parallel and quasi-perpendicular orientations). As a result, we find a high suprathermal ion temperature anisotropy, with the perpendicular to parallel ratio average as high as ~ 2.0 in the subsolar regions, and greater than unity throughout the magnetosheath. This prevailing perpendicular anisotropy, comparable to but slightly larger than typically observed in Earth's magnetosheath (Dimmock et al., 2015), suggests conditions favorable for the growth of Alfvén-ion cyclotron and/or mirror mode instabilities, as at Earth (Soucek et al., 2015).

Given the extensive 3-D coverage of the Mars-solar wind interaction that the MAVEN data set now affords, we can attempt to go beyond basic measurable parameters in order to access macroscopic forces. Many levels of complexity are available to us in describing the forces acting on the plasma populations around Mars, from a simple one-fluid MHD description to a fully kinetic multispecies description. Following Chapman and Dunlop (1986) and Sauer et al. (1994), one can approximate the macroscopic forces acting on the solar wind protons and heavy planetary ions using a two-fluid approximation for the coupled momentum equations.

$$\vec{F}_p = m_p n_p \left(\frac{\partial}{\partial t} + \vec{v}_p \cdot \nabla \right) \vec{v}_p = \frac{n_p}{n_e} \left[q n_h (\vec{v}_p - \vec{v}_h) \times \vec{B} + \vec{J} \times \vec{B} - \nabla P_e \right] - \nabla \cdot \vec{P}_p \quad (1)$$

$$\vec{F}_h = m_h n_h \left(\frac{\partial}{\partial t} + \vec{v}_h \cdot \nabla \right) \vec{v}_h = \frac{n_h}{n_e} \left[q n_p (\vec{v}_h - \vec{v}_p) \times \vec{B} + \vec{J} \times \vec{B} - \nabla P_e \right] - \nabla \cdot \vec{P}_h \quad (2)$$

Equations (1) and (2) incorporate the usual fluid particle pressure (assuming scalar electron pressure P_e and tensor ion pressure \vec{P}_i) and $J \times B$ force terms, with the latter separable into magnetic pressure and curvature/tension terms in the standard fashion, and also include the momentum transfer between the solar wind and heavy ions. This set of coupled equations assumes quasi-neutrality ($n_e = n_p + n_h$) and therefore neglects direct consideration of polarization electric fields. Note that adding the two equations recovers the usual one-fluid MHD momentum equation.

The only term in these equations that we can directly compute from single point measurements is the $v \times B$ momentum transfer term. However, by using statistical ensembles of measurements such as those shown in Figure 5, we can approximate the $J \times B$ and ion pressure gradient terms by taking vector derivatives of vector magnetic field and pressure components on the 3-D grids. For the $J \times B$ term we utilize the 3-D binned maps of the three components of the vector magnetic field and take combinations of derivatives to compute $(\nabla \times \vec{B}) / \mu_0 \times \vec{B}$. Since the derivative of the average clearly does not equal the average of the derivative, we can recover only approximations of the force terms. For the $J \times B$ term in particular, averaging before differentiating can lead to large underestimates of the actual average force, particularly in regions with large magnetic field gradients such as those present at low altitudes and near the magnetotail current sheet. However, these at least suffice to provide a first-order view of the morphology of the forces acting elsewhere in the Mars-solar wind interaction. In the upstream region and magnetosheath, with larger gradient scales, the approximations we utilize should lead to only minor underestimates, although the magnitude of any underestimate remains to be quantitatively analyzed.

Given the limitations in the SWIA FOV, we cannot generally measure the full ion pressure tensor. However, given the data selection process described above, we can always estimate the parallel and one of the perpendicular diagonal terms. Furthermore, we find that in most cases the off-diagonal terms remain small, as expected given their physical interpretation. We therefore construct an approximation to the pressure tensor in magnetic field-aligned coordinates by utilizing only the diagonal terms and assuming equal values for the two perpendicular terms. We then compute the divergence of this tensor in MSE coordinates, utilizing the local average magnetic field vector to perform the coordinate transformation at each point on the grid. Since SWIA cannot distinguish between ions of different species, we emphasize that the SWIA measurements only provide a reasonable approximation of the ion density, pressure, and flow velocity in the upstream and magnetosheath regions, where protons represent the dominant ion species.

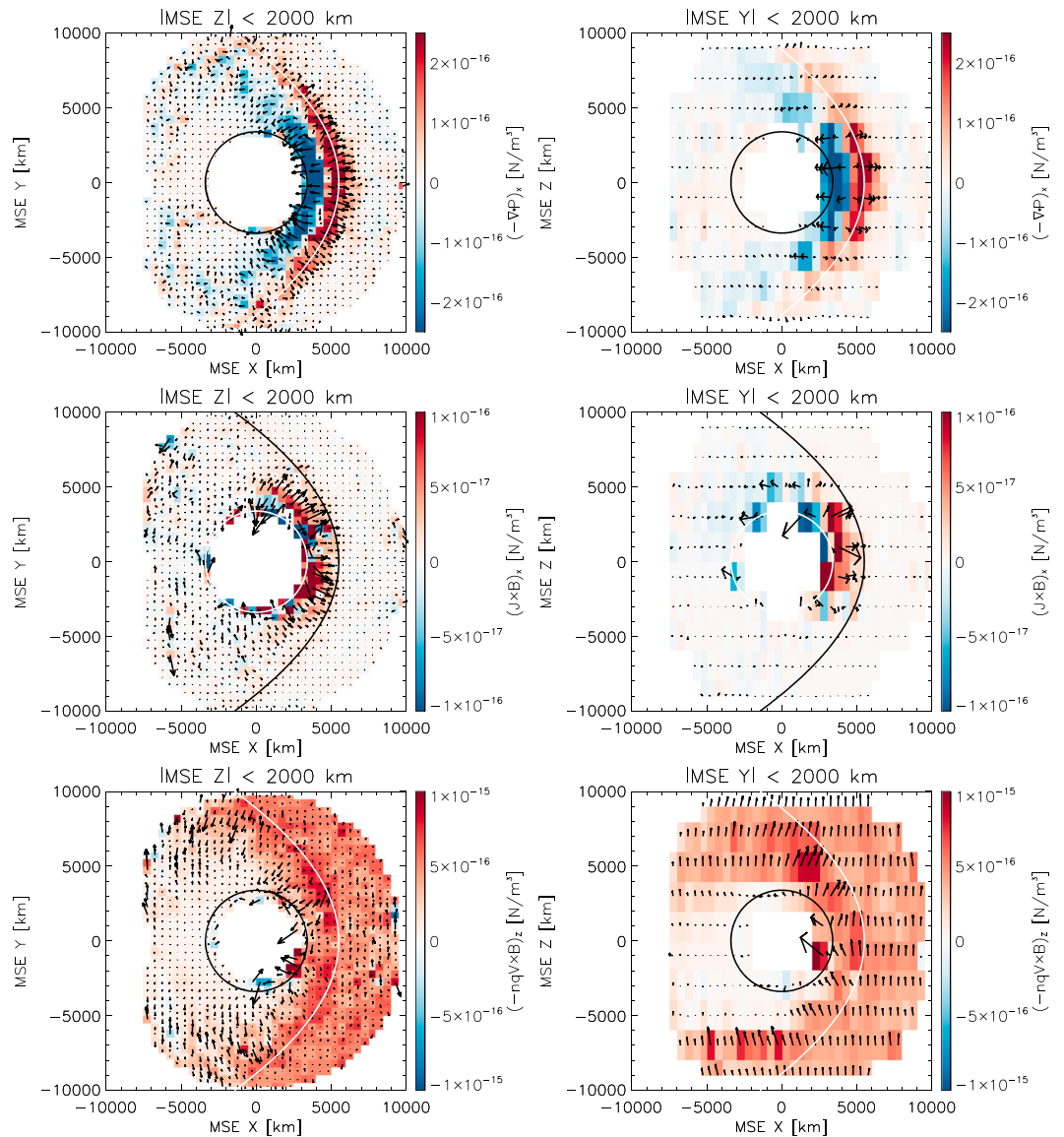


Figure 6. Components of the estimated suprathermal ion pressure gradient, $J \times B$, and $v \times B$ forces derived from the maps of Figure 5, in the (left column) MSE x-y plane and (right column) MSE x-z plane. The arrows indicate normalized in-plane vector components. Note the different color scales for each force term.

We show average values of the three force terms accessible to us from SWIA and MAG measurements in Figure 6, in two orthogonal planes. The results indicate a largely cylindrically symmetric average pressure gradient force, in keeping with the symmetry of the average observed suprathermal ion density, velocity, and temperature. The pressure gradient force acts to decelerate and deflect the incident solar wind flow across the bow shock, and then to reaccelerate it around the obstacle. At lower altitudes, the magnetic pressure associated with the piled up magnetic field acts in part to counterbalance this force (thermal ionospheric and crustal magnetic field pressure may also play a role) and largely prevents the solar wind protons from penetrating the central magnetosphere. The outward $J \times B$ force shown in Figure 6 represents the effects of this magnetic pressure. The overall morphology of these two force terms appears fairly similar to that predicted from simulations of the terrestrial magnetosheath (Wang et al., 2004).

Meanwhile, the antisunward $J \times B$ force near the terminators shows the effects of magnetic curvature/tension forces, which in part act to accelerate planetary heavy ions downstream with the draped magnetic field. Unlike the pressure gradient force, the $J \times B$ force has some asymmetries, with stronger antisunward forces

in the +z hemisphere. This represents an additional manifestation of the hemispheric draping asymmetry discussed by Dubinin et al. (2014) at Mars, and previously shown by Zhang et al. (2010) for Venus.

Finally, the $v \times B$ term shown in the bottom row of Figure 6 represents an estimate of the motional electric field associated with the solar wind flow, which provides the momentum coupling force on the heavy planetary ions in the limit of $n_h \ll n_p$ (the condition for classical ion pickup). In regions with large heavy ion density, the velocity of the heavy ions also plays a role as shown in equations (1) and (2), and the momentum coupling between solar wind and heavy ions leads to a cyclical interchange between the two populations as described by Dubinin et al. (2011). This force maintains nearly the same direction as the motional electric field of the upstream solar wind (the MSE +z direction, by definition), albeit with some deviations due to the flow deflection in the magnetosheath, and it has a roughly symmetric structure in the x-y plane. The magnitude of the force increases slightly in the sheath, since the magnetic field increase more than compensates for the decrease in flow velocity. In the upstream, magnetosheath, and flank regions the $v \times B$ term greatly exceeds the other terms in strength. This corresponds to basic expectations, since the flow remains both supersonic and super-Alfvénic throughout most of the magnetosheath, so the bulk flow of the plasma still plays a dominant role over magnetic and pressure gradient forces. Therefore, any exospheric constituents ionized in these regions of space will at least initially follow classical pickup ion trajectories. Closer to the planet, other forces, including terms we have not considered such as the thermal electron pressure gradient, play more important roles.

4. Variability of the Mars-Solar Wind Interaction

While the maps shown in Figures 5 and 6 represent the average morphology of the Mars-solar wind interaction, we also wish to understand how this interaction varies with solar wind and IMF. We first consider the effect of the upstream IMF orientation, by separating the observations into three cone angle (i.e., the angle between the IMF and the sunward direction) ranges. For our time range, 28% of orbits have cone angles of 0–60° (including the toward-IMF sector), 53% have cone angles of 60–120° (both toward and away sectors), and 19% have cone angles of 120–180° (including the away sector). Figures 7–9 show the same basic measurable and force terms as Figures 5 and 6, for the most sunward (toward) cone angle range and the most antisunward (away) range. In MSE coordinates, the quasi-parallel foreshock lies predominantly on the +y side for cone angles of 0–60°, and on the –y side for cone angles of 120–180°. For comparatively rare near-radial IMF conditions, both sides of the bow shock can have quasi-parallel geometry.

As shown in Figure 7, the IMF orientation organizes the magnetic field draping pattern throughout the interaction region. For both orientations, we observe similar magnetic field pileup and draping patterns in the magnetosphere. However, in the magnetosheath, the magnetic field shows signs of compression farther upstream (essentially at the bow shock) on the quasi-perpendicular flank, while on the quasi-parallel flank it experiences a large rotation before compression occurs (well downstream from the bow shock). This asymmetry appears consistent with that expected from simulations of Mars (Ma et al., 2004; Najib et al., 2011) and Venus (Jarvinen et al., 2013; Kallio et al., 2006). Despite these large-scale draping asymmetries, we observe only minor asymmetries in suprathermal ion density and velocity, consistent with the primarily super-Alfvénic nature of the magnetosheath. We do see hints in these parameters that the bow shock lies farther upstream on the quasi-perpendicular flank than on the quasi-parallel flank, also consistent with previous observations (Zhang et al., 1991) and with Venus simulations (Jarvinen et al., 2013). However, the magnitude of the density and the degree of lateral deflection remain remarkably consistent for different IMF orientations. We note that the apparent asymmetry in the upstream off-axis flow results from the velocity aberration due to the orbital motion of Mars around the Sun, which leads to an off-axis flow in opposite directions in MSE coordinates for the two cone angle ranges shown. For cone angles of 120–180°, we observe possible signs of “preconditioning” (Sibeck et al., 2001) in the form of deflection of the flow ahead of the bow shock in the quasi-parallel foreshock; however, we find no such effect for cone angles of 0–60°.

Although we observe only minimal asymmetries in density and velocity, Figure 8 reveals a large asymmetry in suprathermal ion temperature. While the perpendicular temperature appears symmetric, the parallel temperature has larger values throughout the quasi-parallel foreshock and magnetosheath. As a result, the suprathermal ions have much larger anisotropy on the quasi-perpendicular flank, with dramatically reduced values on the quasi-parallel flank. This asymmetry in temperature anisotropy agrees with that observed in the

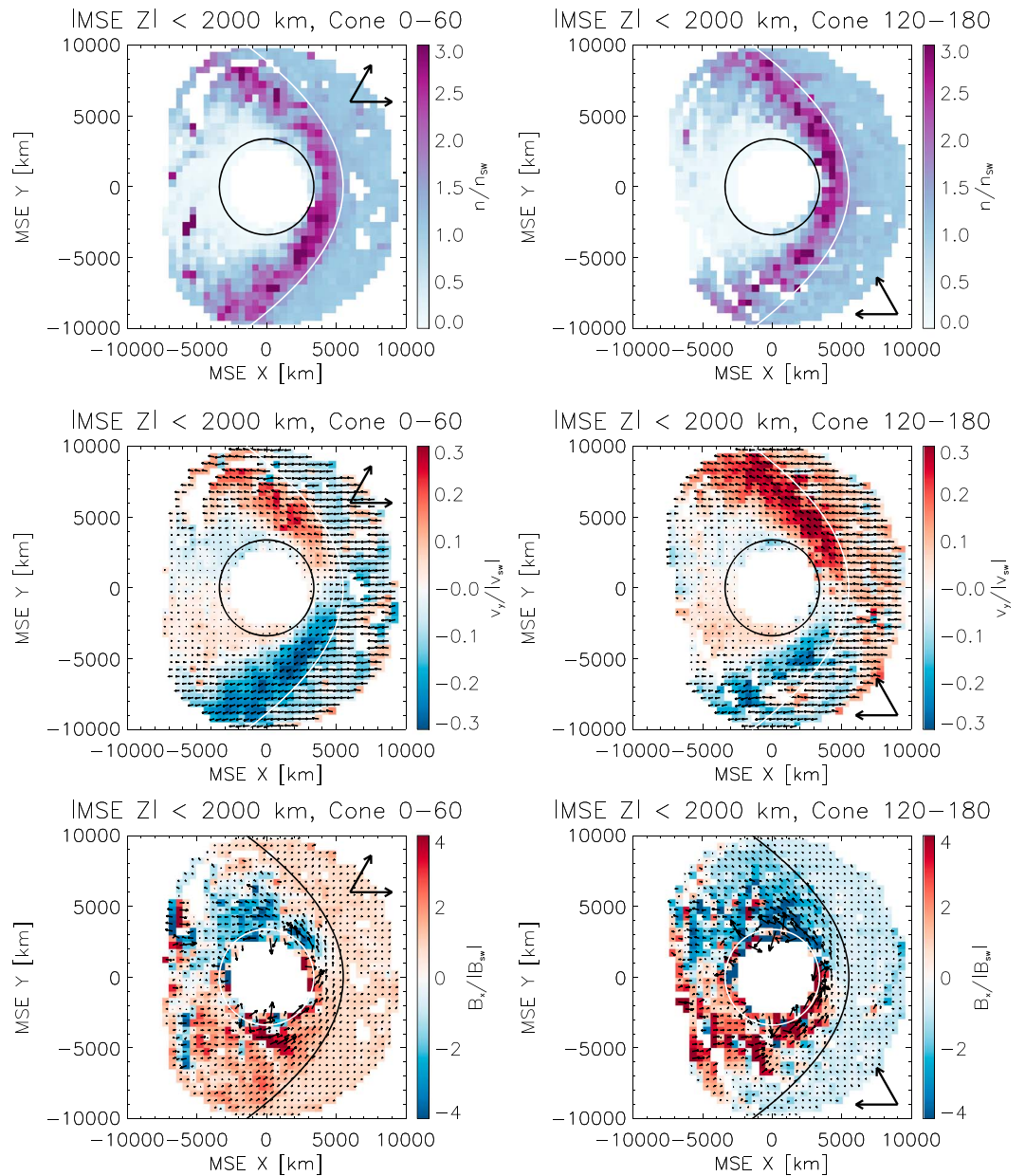


Figure 7. Average suprathermal ion density, magnetic field component B_x , and suprathermal ion velocity component V_y in the MSE x-y plane in the same format as Figure 5, for two different IMF cone angle ranges (as indicated by inset arrows in each panel).

terrestrial magnetosheath (Dimmock et al., 2015). This asymmetry should lead to a corresponding asymmetry in mirror mode occurrence, and it suggests that different families of plasma instabilities can grow and modify the particle distributions on the two flanks of the Martian magnetosphere.

Despite the asymmetries in basic measurable quantities discussed above, the asymmetries in the force terms remain rather modest, as shown in Figure 9. Perhaps in part because the smaller quantity of data in the two selected cone angle ranges leads to an increased level of noise in the numerical derivatives compared to the overall average shown in Figure 6, we find it difficult to conclusively identify any consistent asymmetries in the force terms. However, we note that at least in the MSE x-y plane, several effects may moderate the magnitude of any asymmetries. First, the larger parallel suprathermal ion temperature on the quasi-parallel flank provides a parallel ion pressure gradient that in part compensates for the fact that the perpendicular ion

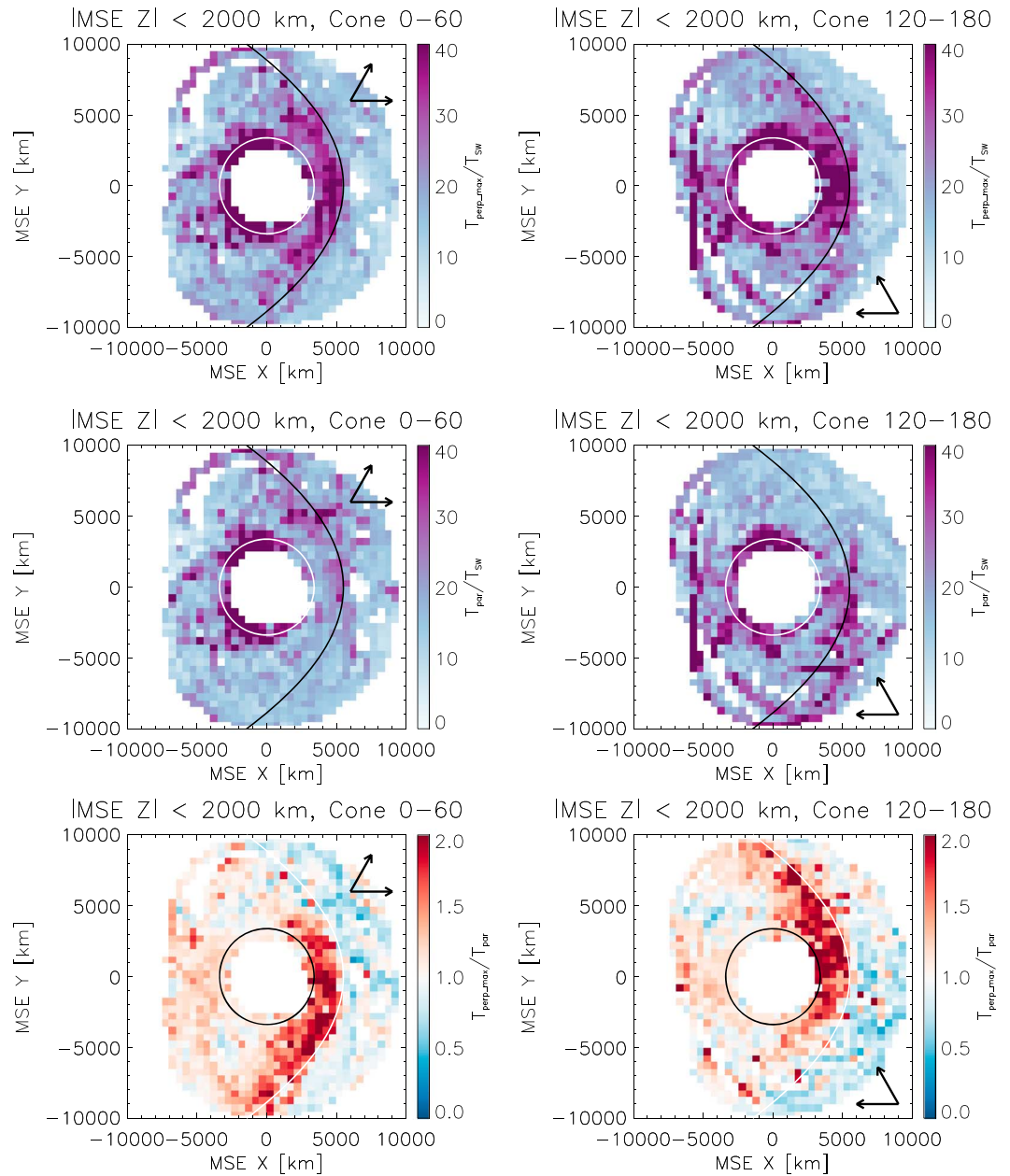


Figure 8. Suprathermal ion temperature components and anisotropy in the MSE x-y plane in the same format as Figure 5, for two different IMF cone angle ranges.

pressure gradient in that region cannot act as efficiently to decelerate the flow. Second, the larger magnitude of the draped magnetic field on the quasi-perpendicular flank leads to a magnetic pressure gradient force that helps counterbalance the larger magnetic tension/curvature forces on the quasi-parallel flank. Therefore, the plasma naturally arranges itself to provide the forces necessary to decelerate and deflect the solar wind flow in a cylindrically symmetric manner, as expected given the essentially symmetric obstacle formed by the Martian ionosphere (note that averaging over all subsolar longitudes removes most of the influence of the asymmetric crustal magnetic fields).

We next consider the effect of the upstream Alfvén Mach number, which we found to have the largest influence on the morphology of the Mars-solar wind interaction of any single controlling factor that we investigated. Within in our time range, 24% of orbits have Mach numbers less than 8, 38% of orbits have

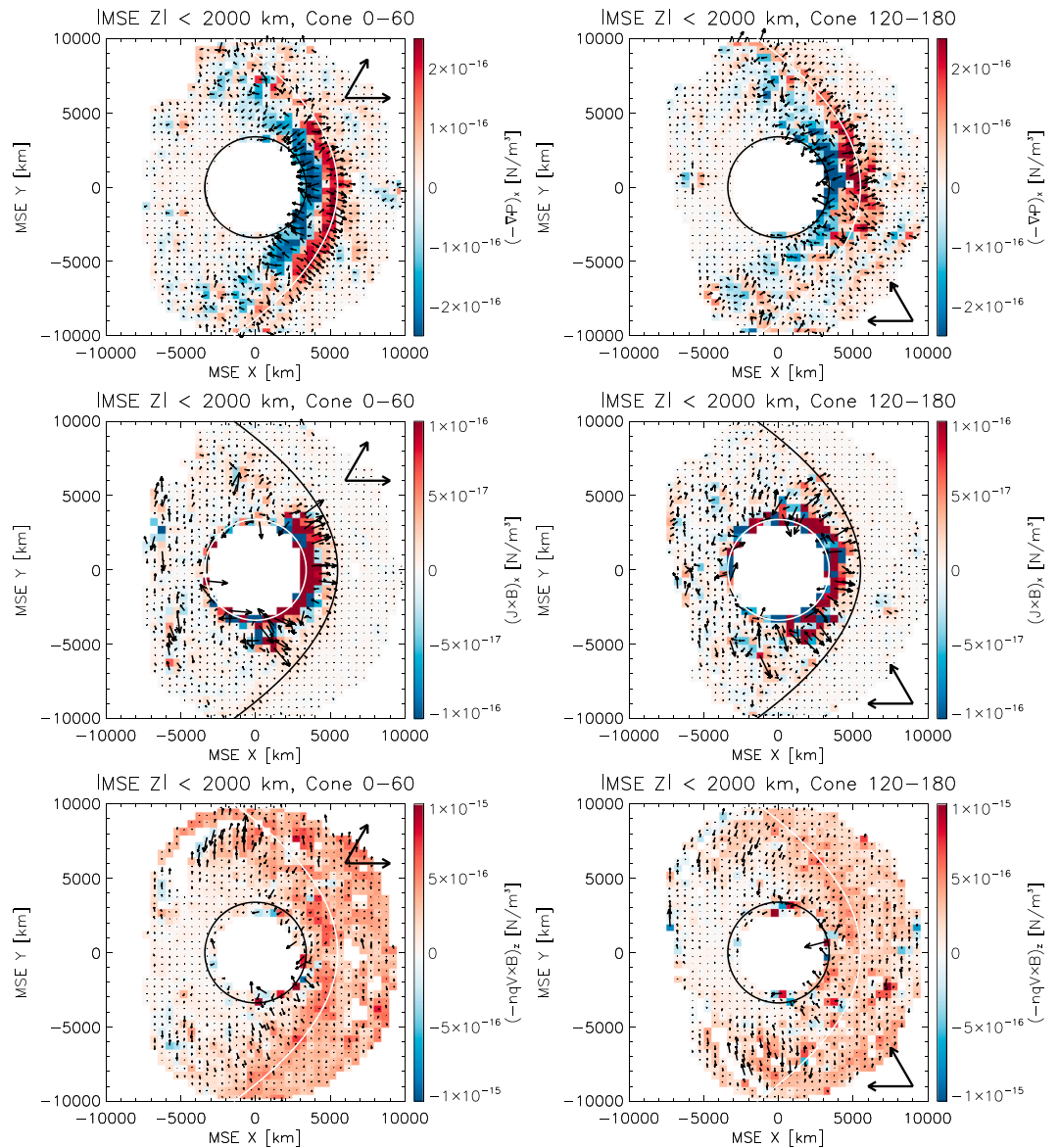


Figure 9. Components of the estimated suprathermal ion pressure gradient, $J \times B$, and $v \times B$ forces in the MSE x - y plane in the same format as Figure 6, for two different IMF cone angle ranges.

Mach numbers between 8 and 12, 29% of orbits have Mach numbers between 12 and 20, and 9% of orbits have Mach numbers greater than 20. These Mach numbers exceed those typically observed at Earth, and greatly exceed those at Venus, thanks to the expansion of the solar wind plasma with distance from the Sun (Russell, Hoppe, & Livesey, 1982). Figures 10–12 show the same basic measurable and force terms as Figures 5–9, for the Mach number ranges $MA < 8$ and $12 < MA < 20$.

As shown in Figure 10, the overall structure of the interaction region changes with Mach number. We observe an overall compression of the magnetosheath and magnetosphere under high Mach number conditions, in agreement with basic physical expectations and with previous studies showing that the Martian bow shock decreases in scale and becomes less flared under high Mach number conditions (Edberg et al., 2010; Halekas et al., 2017). This also manifests itself in a larger normalized magnetic field (i.e., greater pile up/compression of the upstream field) in the magnetosphere under high Mach number conditions, though we note that the absolute magnetic field actually has a greater magnitude under low Mach number conditions. The region of maximum compression and deflection visible in the ion density and velocity also decreases in thickness

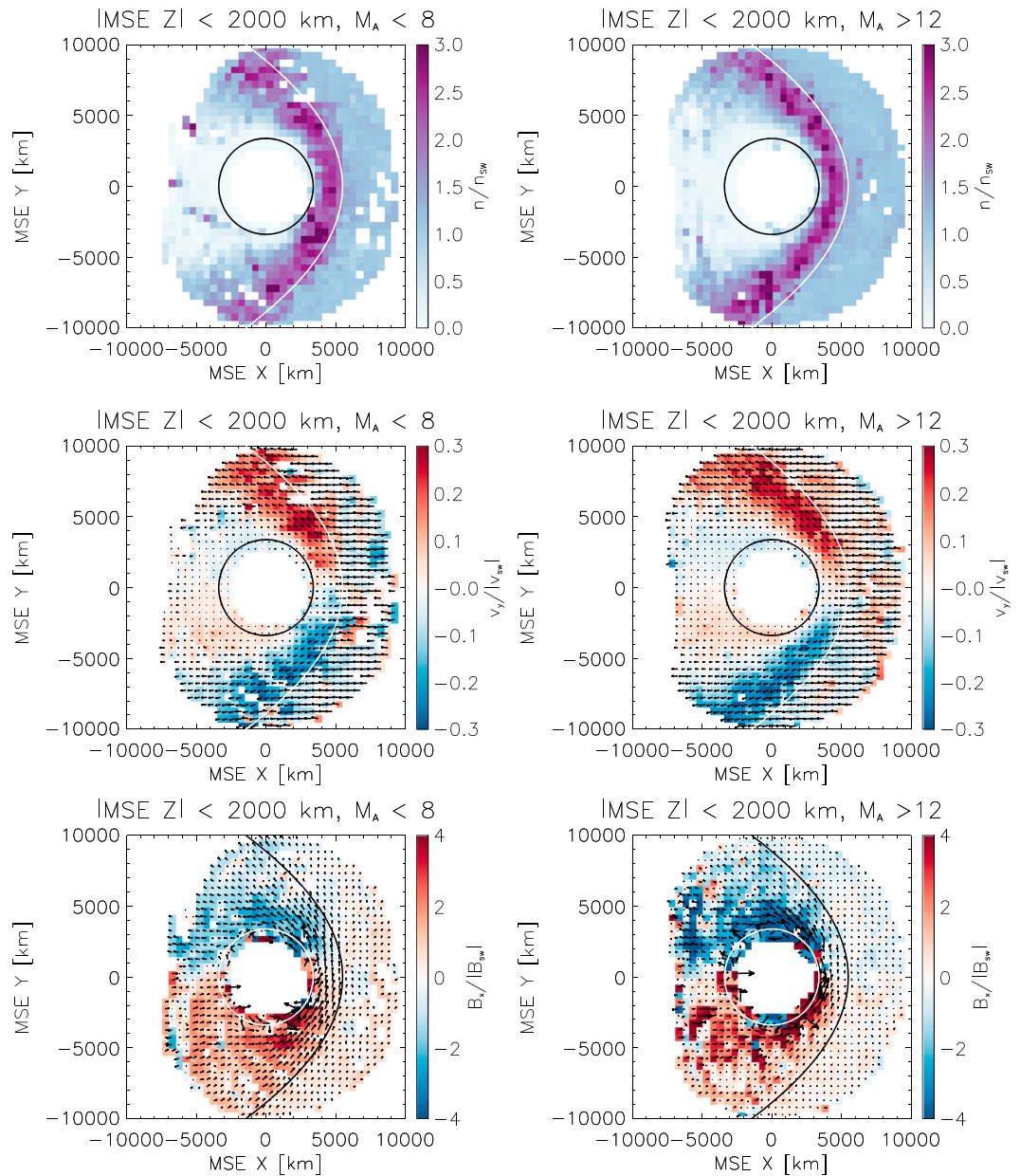


Figure 10. Average suprathermal ion density, magnetic field component B_x , and suprathermal ion velocity component V_y in the MSE x - y plane in the same format as Figures 5 and 7, for two different ranges of solar wind Mach number.

for high Mach number conditions, despite the fact that the ion gyroradius increases with Mach number, suggesting that this occurs due to fluid rather than kinetic effects. Finally, we note some signs of preconditioning of both the upstream flow and magnetic field draping under high Mach number conditions, suggesting that foreshock wave-particle interactions might play an important role in the overall interaction.

The suprathermal ion temperature also changes with the upstream Mach number, as shown in Figure 11, with higher values of both perpendicular and parallel temperature components under high Mach number conditions. Interestingly, though both components increase in magnitude for high Mach numbers, the ion temperature anisotropy has greater values for low Mach numbers (consistent with the highly anisotropic ion temperature observed in the magnetosheath on the orbit of Figure 3). This trend disagrees with the behavior anticipated from the double adiabatic equations, given the larger magnetic field compression

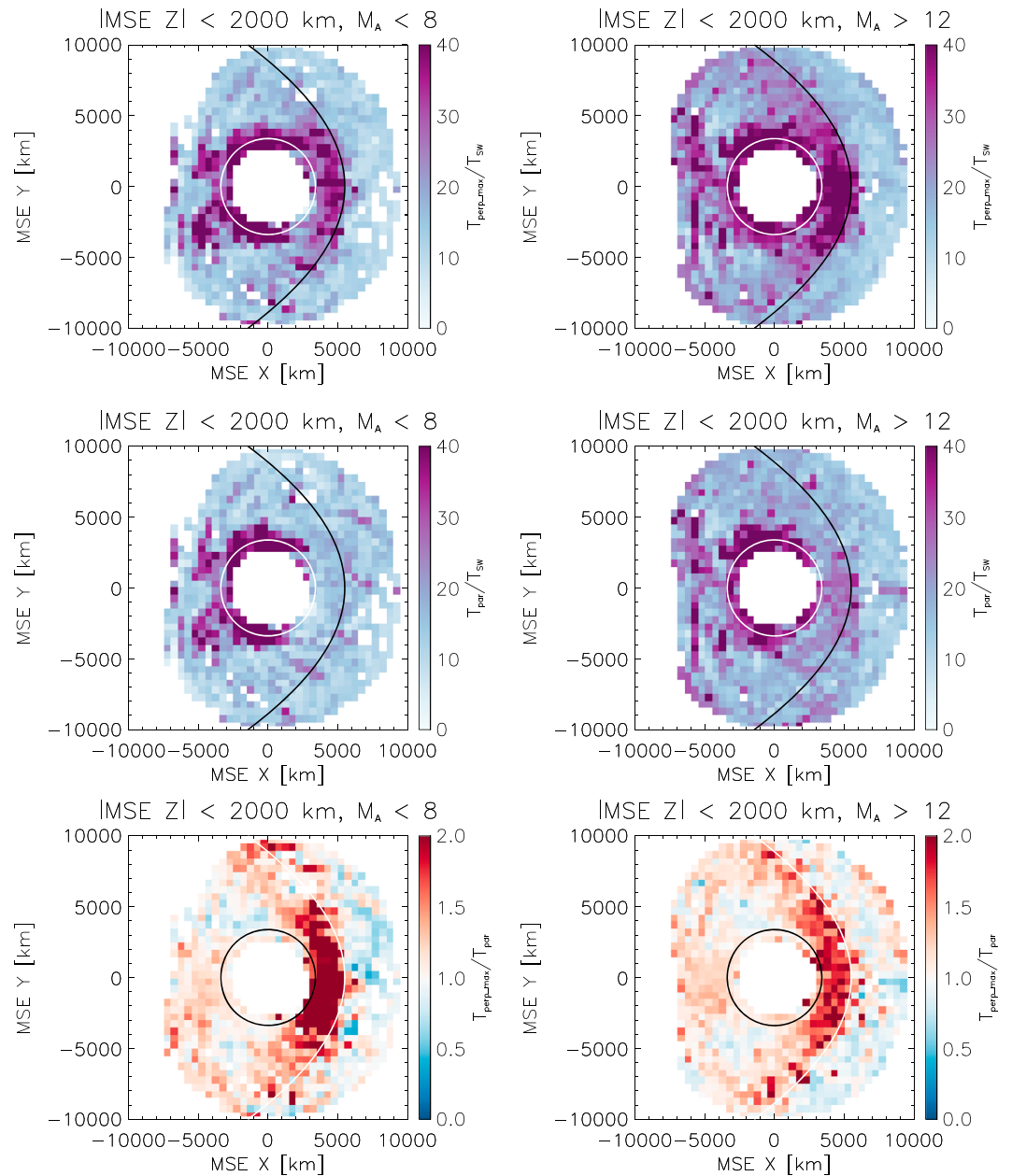


Figure 11. Suprathermal ion temperature components and anisotropy in the MSE x-y plane in the same format as Figures 5 and 8, for two different ranges of solar wind Mach number.

but comparable density compression observed in the high Mach number case. Instead, this trend likely results from differences in the mitigating effects of wave-particle interactions. Low solar wind Mach numbers correspond to lower values of ion β in the magnetosheath, with the result that both the ion cyclotron and mirror mode instabilities have higher threshold values of temperature anisotropy (Gary et al., 1993), implying that larger values of anisotropy can occur in low Mach number conditions before wave-particle interactions act to remove the anisotropy. Similar effects occur in the terrestrial magnetosheath, which also has higher ion temperature anisotropy for low Mach number conditions (Dimmock et al., 2015). We expect that this should also translate to a higher occurrence of mirror mode instabilities, as at the Earth.

Finally, we show the effect of upstream Mach number on the basic force terms, in Figure 12. We observe a minimal effect on the suprathermal ion pressure gradient force, with the main observable signature a

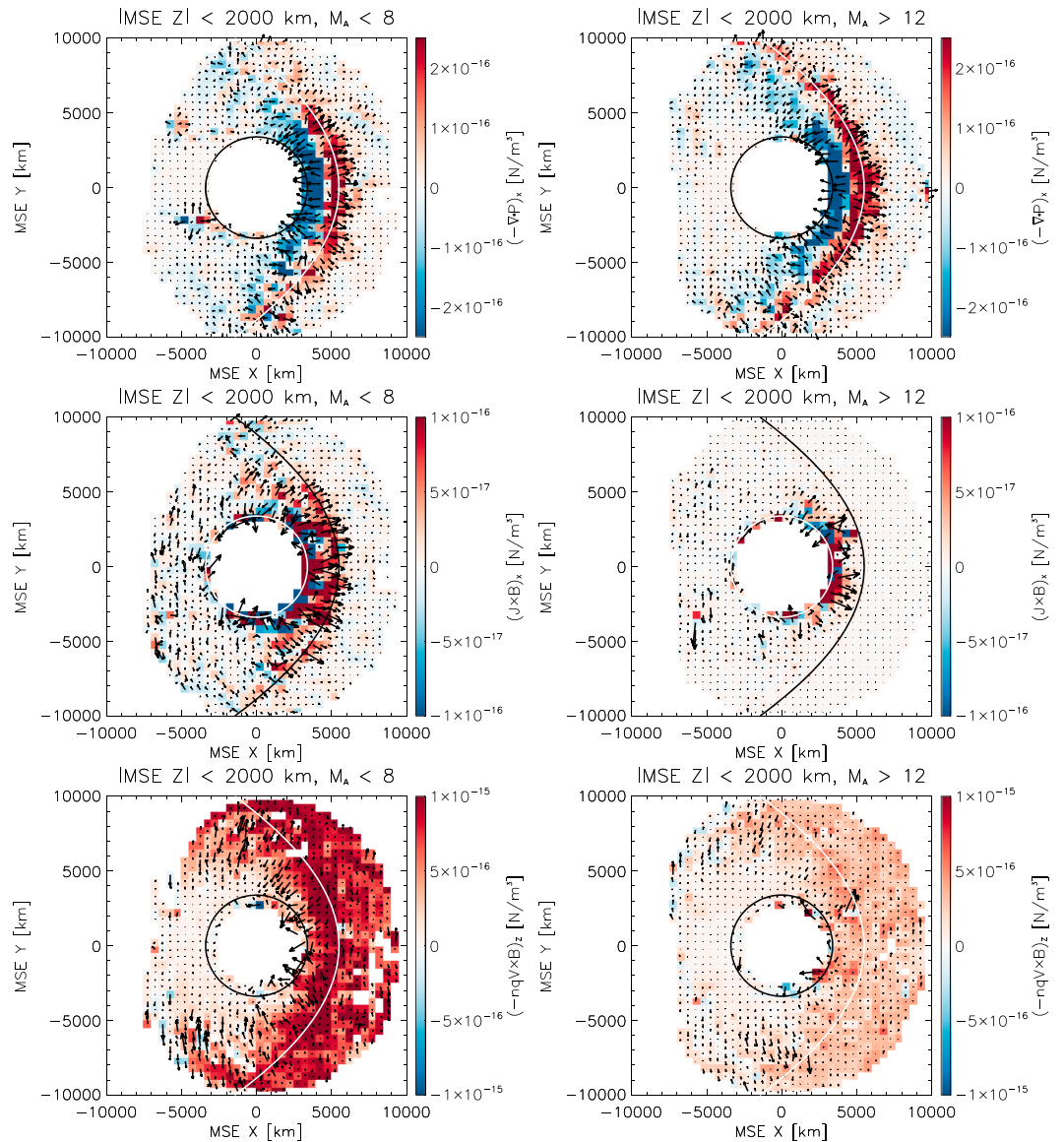


Figure 12. Components of the estimated suprathermal ion pressure gradient, $J \times B$, and $v \times B$ forces in the MSE x-y plane in the same format as Figures 6 and 9, for two different ranges of solar wind Mach number.

change in size and reduction in thickness of the region with large pressure gradient forces, consistent with the observed changes in the ion density and temperature. On the other hand, both the $J \times B$ and $v \times B$ terms increase dramatically during low Mach number conditions, due to the larger magnetic field magnitude. Furthermore, the region with significant $J \times B$ forces expands to fill essentially the entire magnetosheath for low Mach numbers, in contrast to the high Mach conditions during which the magnetic forces prove appreciable only in the magnetic pileup region within the magnetosheath. In the low Mach number case, magnetic forces can exceed ion pressure gradient forces in some regions, potentially causing significant plasma acceleration and magnetospheric asymmetries similar to those observed at the Earth under low Mach number conditions (Lavraud et al., 2007, 2013).

5. Conclusions

The MAVEN mission provides us with a unique platform for the study of the Mars-solar wind interaction. This initial study demonstrates that despite the fact that this interaction has unique aspects not present at the

Earth, many similarities still exist, particularly in the most directly comparable magnetosheath and upstream regions of the interaction. Just as at Earth, the magnetosheath has IMF-controlled asymmetries in both magnetic field draping and ion flow patterns, which correspond to asymmetries in the macroscopic forces exerted on the plasma. Also, as at Earth, the compression of the flow and addition of reflected ions to the distribution lead to large increases in the measured ion temperature, and significant temperature anisotropies occur throughout much of the magnetosheath. The magnitude of these anisotropies varies with both IMF orientation and upstream Mach number, which will affect the growth and evolution of wave-particle instabilities and the subsequent modification of charged particle distributions. These physical effects therefore have important implications for the transport and dissipation of energy throughout the Mars-solar wind interaction. In the future, we should go beyond this initial study to include the effects of planetary ion populations, suprathermal electrons, thermal ionospheric plasma, and crustal magnetic fields in order to understand the overall force balance throughout the Martian magnetosphere, as well as its variability with season and solar cycle. MAVEN provides all the necessary measurements for such a study, and with further extended mission observations will continue to contribute to our understanding of this interaction. Furthermore, detailed comparisons of the morphology, magnitude, and direction of the quantities both directly measured by and derived from MAVEN with global plasma simulations will help elucidate the roles of the various charged particles, fields, and forces in the Mars-solar wind interaction.

Acknowledgments

We acknowledge the MAVEN contract for support. All MAVEN data are available on the Planetary Data System (<https://pds.nasa.gov>).

References

- Bertucci, C., Duru, F., Edberg, N., Fraenz, M., Martinecz, C., Szego, K., & Vaisberg, O. (2011). The induced magnetospheres of Mars, Venus, and Titan. *Space Science Reviews*, *162*(1–4), 113–171. <https://doi.org/10.1007/s11214-011-9845-1>
- Bertucci, C., Mazelle, C., Crider, D. H., Mitchell, D. L., Sauer, K., Acuña, M. H., ... Winterhalter, D. (2004). MGS MAG/ER observations at the magnetic pileup boundary of Mars: Draping enhancement and low frequency waves. *Advances in Space Research*, *33*(11), 1938–1944. <https://doi.org/10.1016/j.asr.2003.04.054>
- Boesswetter, A., Bagdonat, T., Motschmann, U., & Sauer, K. (2004). Plasma boundaries at Mars: A 3-D simulation study. *Annales Geophysicae*, *22*(12), 4363–4379. <https://doi.org/10.5194/angeo-22-4363-2004>
- Brain, D., Barabash, S., Boesswetter, A., Bougher, S., Brecht, S., Chanteur, G., ... Terada, N. (2010). A comparison of global models for the solar wind interaction with Mars. *Icarus*, *206*(1), 139–151. <https://doi.org/10.1016/j.icarus.2009.06.030>
- Brain, D. A., Halekas, J. S., Lillis, R. J., Mitchell, D. L., Lin, R. P., & Crider, D. H. (2005). Variability of the altitude of the Martian sheath. *Geophysical Research Letters*, *32*, L18203. <https://doi.org/10.1029/2005GL023126>
- Brecht, S. H., & Ledvina, S. A. (2007). The solar wind interaction with the Martian ionosphere/atmosphere. *Space Science Reviews*, *126*(1–4), 15–38. <https://doi.org/10.1007/s11214-006-9084-z>
- Chapman, S. C., & Dunlop, M. W. (1986). Ordering of momentum transfer along VvB in the AMPTE solar wind releases. *Journal of Geophysical Research*, *91*(A7), 8051–8055. <https://doi.org/10.1029/JA091iA07p08051>
- Chew, G. F., Goldberger, M. L., & Low, F. E. (1956). The Boltzmann equation and the one-fluid hydromagnetic equations in the absence of particle collisions. *Proceedings of the Royal Society of London. Series A*, *236*(1204), 112–118. <https://doi.org/10.1098/rspa.1956.0116>
- Connerney, J. E. P., Espley, J., Lawton, P., Murphy, S., Odum, J., Oliverson, R., & Sheppard, D. (2015). The MAVEN magnetic field investigation. *Space Science Reviews*, *195*(1–4), 257–291. <https://doi.org/10.1007/s11214-015-0169-4>
- Connerney, J. E. P., Espley, J. R., DiBraccio, G. A., Gruesbeck, J. R., Oliverson, R. J., Mitchell, D. L., ... Jakosky, B. M. (2015). First results of the MAVEN magnetic field investigation. *Geophysical Research Letters*, *42*, 8819–8827. <https://doi.org/10.1002/2015GL065366>
- Crider, D., Brain, D. A., Acuña, M., Vignes, D., Mazelle, C., & Bertucci, C. (2004). Mars Global Surveyor observations of solar wind magnetic field draping around Mars. *Space Science Reviews*, *111*(1/2), 203–221. <https://doi.org/10.1023/B:SPAC.0000032714.66124.4e>
- Crooker, N. U., & Siscoe, G. L. (1977). A mechanism for pressure anisotropy and mirror instability in the dayside magnetosheath. *Journal of Geophysical Research*, *82*(1), 185–186. <https://doi.org/10.1029/JA082i001p0185>
- Dimmock, A. P., Osmane, A., Pulkkinen, T. I., & Nykyri, K. (2015). A statistical study of the dawn-dusk asymmetry of ion temperature anisotropy and mirror mode occurrence in the terrestrial dayside magnetosheath using THEMIS data. *Journal of Geophysical Research: Space Physics*, *120*, 5489–5503. <https://doi.org/10.1002/2015JA021192>
- Dong, C., Bougher, S. W., Ma, Y., Toth, G., Lee, Y., Nagy, A. F., ... Najib, D. (2015). Solar wind interaction with the Martian upper atmosphere: Crustal field orientation, solar cycle, and seasonal variations. *Journal of Geophysical Research: Space Physics*, *120*, 7857–7872. <https://doi.org/10.1002/2015JA020990>
- Dong, C., Bougher, S. W., Ma, Y., Toth, G., Nagy, A. F., & Najib, D. (2014). Solar wind interaction with Mars upper atmosphere: Results from the one-way coupling between the multifluid MHD model and the MTGCM model. *Geophysical Research Letters*, *41*, 2708–2715. <https://doi.org/10.1002/2014GL059515>
- Dubinin, E., Fraenz, M., Fedorov, A., Lundin, R., Edberg, N., Duru, F., & Vaisberg, O. (2011). Ion energization and escape on Mars and Venus. *Space Science Reviews*, *162*(1–4), 173–211. <https://doi.org/10.1007/s11214-011-9831-7>
- Dubinin, E., Fraenz, M., Zhang, T. L., Woch, J., & Wei, Y. (2014). Magnetic fields in the Mars ionosphere of a noncrustal origin: Magnetization features. *Geophysical Research Letters*, *41*, 6329–6334. <https://doi.org/10.1002/2014GL061453>
- Dubinin, E., Franz, M., Woch, J., Roussos, E., Barabash, S., Lundin, R., ... Acuna, M. (2006). Plasma morphology at Mars: ASPERA-3 observations. *Space Science Reviews*, *126*, 209–238.
- Dubinin, E., Lundin, R., Koskinen, H., & Norberg, O. (1993). Cold ions at the Martian bow shock: Phobos observations. *Journal of Geophysical Research*, *98*(A4), 5617–5623. <https://doi.org/10.1029/92JA02374>
- Dubinin, E., Modolo, R., Fraenz, M., Woch, J., Duru, F., Akalin, F., ... Picardi, G. (2008). Structure and dynamics of the solar wind/ionosphere interface on Mars: MEX-ASPERA-3 and MEX-MARSIS observations. *Geophysical Research Letters*, *35*, L11103. <https://doi.org/10.1029/2008GL033730>

- Dubinin, E., Sauer, K., Baumgärtel, K., & Lundin, R. (1997). The Martian magnetosheath: Phobos-2 observations. *Advances in Space Research*, 20(2), 149–153. [https://doi.org/10.1016/S0273-1177\(97\)00525-5](https://doi.org/10.1016/S0273-1177(97)00525-5)
- Dubinin, E., Sauer, K., Delva, M., & Tanaka, T. (1998). The IMF control of the Martian bow shock and plasma flow in the magnetosheath. Predictions of 3-d simulations and observations. *Earth, Planets and Space*, 50(10), 873–882. <https://doi.org/10.1186/BF03352181>
- Edberg, N., Brain, D. A., Lester, M., Cowley, S. W. H., Modolo, R., Fraenz, M., & Barabash, S. (2009). Plasma boundary variability at Mars as observed by Mars Global Surveyor and Mars Express. *Annales Geophysicae*, 27(9), 3537–3550. <https://doi.org/10.5194/angeo-27-3537-2009>
- Edberg, N. J. T., Lester, M., Cowley, S. W. H., & Eriksson, A. I. (2008). Statistical analysis of the location of the Martian magnetic pileup boundary and bow shock and the influence of crustal magnetic fields. *Journal of Geophysical Research*, 113, A08206. <https://doi.org/10.1029/2008JA013096>
- Edberg, N. J. T., Lester, M., Crowley, S. W. H., Brain, D. A., Franz, M., & Barabash, S. (2010). Magnetosonic Mach number effect of the position of the bow shock at Mars in comparison to Venus. *Journal of Geophysical Research*, 115, A07203. <https://doi.org/10.1029/2009JA014998>
- Espley, J. R., Cloutier, P. A., Brain, D. A., Crider, D. H., & Acuña, M. H. (2004). Observations of low-frequency magnetic oscillations in the Martian magnetosheath, magnetic pileup region, and tail. *Journal of Geophysical Research*, 109, A07213. <https://doi.org/10.1029/2003JA010193>
- Fang, X., Ma, Y., Masunaga, K., Dong, Y., Brain, D., Halekas, J., ... Dong, C. (2017). The Mars crustal magnetic field control of plasma boundary locations and atmospheric loss: MHD prediction and comparison with MAVEN. *Journal of Geophysical Research: Space Physics*, 122, 4117–4137. <https://doi.org/10.1002/2016JA023509>
- Fowler, C. M., Andersson, L., Halekas, J., Espley, J. R., Mazelle, C., Coughlin, E. R., ... Jakosky, B. (2017). Electric and magnetic variations in the near Mars environment. *Journal of Geophysical Research*, 122, 8536–8559. <https://doi.org/10.1002/2016JA023411>
- Fraenz, M., Dubinin, E., Roussos, E., Woch, J., Winningham, J. D., Frahm, R., ... Lundin, R. (2006). Plasma moments in the environment of Mars. *Space Science Reviews*, 126, 165–207.
- Gary, S. P., Fuselier, S. A., & Anderson, B. J. (1993). Ion anisotropy instabilities in the magnetosheath. *Journal of Geophysical Research*, 98(A2), 1481–1488. <https://doi.org/10.1029/92JA01844>
- Gosling, J. T., Thomsen, M. F., Bame, S. J., Feldman, W. C., Paschmann, G., & Scokopke, N. (1982). Evidence for specularly reflected ions upstream from the quasi-parallel bow shock. *Geophysical Research Letters*, 9(12), 1333–1336. <https://doi.org/10.1029/GL0091012p01333>
- Hada, T., Oonishi, M., Lembège, B., & Savoini, P. (2003). Shock front nonstationarity of supercritical perpendicular shocks. *Journal of Geophysical Research*, 108(A6), 1233. <https://doi.org/10.1029/2002JA009339>
- Halekas, J. S., Ruhunusiri, S., Harada, Y., Collinson, G., Mitchell, D. L., Mazelle, C., ... Jakosky, B. M. (2017). Structure, dynamics, and seasonal variability of the Mars-solar wind interaction: MAVEN Solar Wind Ion Analyzer in-flight performance and science results. *Journal of Geophysical Research: Space Physics*, 122, 547–578. <https://doi.org/10.1002/2016JA023167>
- Halekas, J. S., Taylor, E. R., Dalton, G., Johnson, G., Curtis, D. W., McFadden, J. P., ... Jakosky, B. M. (2015). The Solar Wind Ion Analyzer for MAVEN. *Space Science Reviews*, 195(1-4), 125–151. <https://doi.org/10.1007/s11214-013-0029-z>
- Hill, P., Paschmann, G., Treumann, R. A., Baumjohann, W., Scokopke, N., & Lühr, H. (1995). Plasma and magnetic field behavior across the magnetosheath near local noon. *Journal of Geophysical Research*, 100(A6), 9575–9583. <https://doi.org/10.1029/94JA03194>
- Jakosky, B. M., Lin, R. P., Grebowsky, J. M., Luhmann, J. G., Mitchell, D. F., Beutelschies, G., ... Zurek, R. (2015). The Mars Atmosphere and Volatile Evolution (MAVEN) mission. *Space Science Reviews*, 195(1-4), 3–48. <https://doi.org/10.1007/s11214-015-0139-x>
- Jarvinen, R., Kallio, E., & Dyadechkin, S. (2013). Hemispheric asymmetries of the Venus plasma environment. *Journal of Geophysical Research: Space Physics*, 118, 4551–4563. <https://doi.org/10.1002/jgra.50387>
- Kallio, E., Jarvinen, R., & Janhunen, P. (2006). Venus-solar wind interaction: Asymmetries and the escape of O^+ ions. *Planetary and Space Science*, 54(13-14), 1472–1481. <https://doi.org/10.1016/j.pss.2006.04.030>
- Kallio, E., Koskinen, H., Barabash, S., Lundin, R., Norberg, O., & Luhmann, J. G. (1994). Proton flow in the Martian magnetosheath. *Geophysical Research Letters*, 99(A12), 23,547–23,559. <https://doi.org/10.1029/94JA01716>
- Lavraud, B., Borovsky, J. E., Ridley, A. J., Pogue, E. W., Thomsen, M. F., Rème, H., ... Lucek, E. A. (2007). Strong bulk plasma acceleration in Earth's magnetosheath: A magnetic slingshot effect? *Geophysical Research Letters*, 34, L14102. <https://doi.org/10.1029/2007GL030024>
- Lavraud, B., Larroque, E., Budnik, E., Génot, V., Borovsky, J. E., Dunlop, M. W., ... Rème, H. (2013). Asymmetry of magnetosheath flows and magnetopause shape during low Alfvén Mach number solar wind. *Journal of Geophysical Research: Space Physics*, 118, 1089–1100. <https://doi.org/10.1002/jgra.50145>
- Luhmann, J. G., Acuña, M. H., Purucker, M., Russell, C. T., & Lyon, J. G. (2002). The Martian magnetosheath: How Venus-like? *Planetary and Space Science*, 50(5-6), 489–502. [https://doi.org/10.1016/S0032-0633\(02\)00028-4](https://doi.org/10.1016/S0032-0633(02)00028-4)
- Ma, Y., Fang, X., Russell, C. T., Nagy, A. F., Toth, G., Luhmann, J. G., ... Dong, C. (2014). Effects of crustal field rotation on the solar wind plasma interaction with Mars. *Geophysical Research Letters*, 41, 6563–6569. <https://doi.org/10.1002/2014GL060785>
- Ma, Y., Nagy, A. F., Sokolov, I. V., & Hansen, K. C. (2004). Three-dimensional, multispecies, high spatial resolution MHD studies of the solar wind interaction with Mars. *Journal of Geophysical Research*, 109, A07211. <https://doi.org/10.1029/2003JA010367>
- Mazelle, C., Winterhalter, D., Sauer, K., Winterhalter, D., Sauer, K., Trotignon, J. G., ... Slavin, J. (2004). Bow shock and upstream phenomena at Mars. *Space Science Reviews*, 111(1/2), 115–181. <https://doi.org/10.1023/B:SPAC.0000032717.98679>
- Mitchell, D. L., Mazelle, C., Sauvaud, J. A., Toublanc, D., Thocaven, R., Federov, A., ... Curtis, D. W. (2016). The MAVEN Solar Wind Electron Analyzer (SWEA). *Space Science Reviews*, 200(1-4), 495–528. <https://doi.org/10.1007/s11214-015-0232-1>
- Modolo, R., Chanteur, G., Dubinin, E., & Matthews, A. P. (2006). Simulated solar wind plasma interaction with the Martian exosphere: Influence of the solar EUV flux on the bow shock and the magnetic pile-up boundary. *Annales Geophysicae*, 24(12), 3403–3410. <https://doi.org/10.5194/angeo-24-3403-2006>
- Modolo, R., Hess, S., Mancini, M., Leblanc, F., Chaufray, J.-Y., Brain, D., ... Mazelle, C. (2016). Mars-solar wind interaction: LatHyS, an improved parallel 3-D multispecies hybrid model. *Journal of Geophysical Research: Space Physics*, 121, 6378–6399. <https://doi.org/10.1002/2015JA022324>
- Moses, S. L., Coroniti, F. V., & Scarf, F. L. (1988). Expectations for the microphysics of the Mars-solar wind interaction. *Geophysical Research Letters*, 15(5), 429–432. <https://doi.org/10.1029/GL015i005p00429>
- Nagy, A. F., Winterhalter, D., Sauer, K., Cravens, T. E., Brecht, S., Mazelle, C., ... Trotignon, J. G. (2004). The plasma environment of Mars. *Space Science Reviews*, 111(1/2), 33–114. <https://doi.org/10.1023/B:SPAC.0000032718.47512.92>
- Najib, D., Nagy, A. F., Tóth, G., & Ma, Y. (2011). Three-dimensional, multifluid, high spatial resolution MHD model studies of the solar wind interaction with Mars. *Journal of Geophysical Research*, 116, A05204. <https://doi.org/10.1029/2010JA016272>
- Paschmann, G., Scokopke, N., Bame, S. J., & Gosling, J. (1982). Observations of gyrating ions in the foot of the nearly perpendicular bow shock. *Geophysical Research Letters*, 9(8), 881–884. <https://doi.org/10.1029/GL0091008p00881>
- Romanelli, N., Mazelle, C., Chaufray, J. Y., Meziane, K., Shan, L., Ruhunusiri, S., ... Jakosky, B. M. (2016). Proton cyclotron waves occurrence rate upstream from Mars observed by MAVEN: Associated variability of the Martian upper atmosphere. *Journal of Geophysical Research: Space Physics*, 121, 11,113–11,128. <https://doi.org/10.1002/2016JA023270>

- Ruhunusiri, S., Halekas, J. S., Connerney, J. E. P., Espley, J. R., McFadden, J. P., Larson, D. E., ... Jakosky, B. M. (2015). Low-frequency waves in the Martian magnetosphere and their response to upstream solar wind driving conditions. *Geophysical Research Letters*, *42*, 8917–8924. <https://doi.org/10.1002/2015GL064968>
- Ruhunusiri, S., Halekas, J. S., Espley, J. R., Mazelle, C., Brain, D., Harada, Y., ... Howes, G. G. (2017). Characterization of turbulence in the Mars plasma environment with MAVEN observations. *Journal of Geophysical Research*, *122*, 656–674. <https://doi.org/10.1002/2016JA023456>
- Russell, C. T., Hoppe, M. M., & Livesey, W. A. (1982). Overshoots in planetary bow shocks. *Nature*, *296*(5852), 45–48. <https://doi.org/10.1038/296045a0>
- Russell, C. T., Luhmann, J. G., Schwingenschuh, K., Riedler, W., & Yeroshenko, Y. (1990). Upstream waves at Mars: Phobos observations. *Geophysical Research Letters*, *17*(6), 897–900. <https://doi.org/10.1029/GL017i006p00897>
- Sagdeev, R. Z., Shapiro, V. D., Shevchenko, V. I., Zacharov, A., Kiraly, P., Szego, K., ... Grard, R. (1990). Wave activity in the neighborhood of the bow shock of Mars. *Geophysical Research Letters*, *17*(6), 893–896. <https://doi.org/10.1029/GL017i006p00893>
- Sauer, K., Bogdanov, A., & Baumgärtel, K. (1994). Evidence of an ion composition boundary (protonopause) in bi-ion fluid simulations of solar wind mass loading. *Geophysical Research Letters*, *21*(20), 2255–2258. <https://doi.org/10.1029/94GL01691>
- Schwartz, S. J., & Burgess, D. (1991). Quasi-parallel shocks: A patchwork of three-dimensional structures. *Geophysical Research Letters*, *18*(3), 373–376. <https://doi.org/10.1029/91GL00138>
- Sckopke, N., Paschmann, G., Bame, S. J., Gosling, J. T., & Russell, C. T. (1983). Evolution of ion distributions across the nearly perpendicular bow shock—Specularly and non-specularly reflected gyrating ions. *Journal of Geophysical Research*, *88*(A8), 6121–6136. <https://doi.org/10.1029/JA088iA08p06121>
- Sckopke, N., Paschmann, G., Brinca, A. L., Carlson, C. W., & Lühr, H. (1990). Ion thermalization in quasi-perpendicular shocks involving reflected ions. *Journal of Geophysical Research*, *95*(A5), 6337–6352. <https://doi.org/10.1029/JA095iA05p06337>
- Sibeck, D. G., Decker, R. B., Mitchell, D. G., Lazarus, A. J., Lepping, R. P., & Szabo, A. (2001). Solar wind preconditioning in the flank foreshock: IMP 8 observations. *Journal of Geophysical Research*, *106*(A10), 21,675–21,688. <https://doi.org/10.1029/2000JA000417>
- Soucek, J., Escoubet, C. P., & Grison, B. (2015). Magnetosheath plasma stability and ULF wave occurrence as a function of location in the magnetosheath and upstream bow shock parameters. *Journal of Geophysical Research: Space Physics*, *120*, 2838–2850. <https://doi.org/10.1002/2015JA021087>
- Trotignon, J., Mazelle, C., Bertucci, C., & Acuña, M. (2006). Martian shock and magnetic pile-up boundary positions and shapes determined from the Phobos 2 and Mars Global Surveyor data sets. *Planetary and Space Science*, *54*(4), 357–369. <https://doi.org/10.1016/j.pss.2006.01.003>
- Vaisberg, O. L. (1992). The solar wind interaction with Mars: A review of results from previous Soviet missions to Mars. *Advances in Space Research*, *12*(9), 137–161. [https://doi.org/10.1016/0273-1177\(92\)90328-U](https://doi.org/10.1016/0273-1177(92)90328-U)
- Wang, Y. L., Raeder, J., & Russell, C. T. (2004). Plasma depletion layer: Magnetosheath flow structure and forces. *Annales Geophysicae*, *22*(3), 1001–1017. <https://doi.org/10.5194/angeo-22-1001-2004>
- Zhang, T. L., Baumjohann, W., Du, J., Nakamura, R., Jarvinen, R., Kallio, E., ... Russell, C. T. (2010). Hemispheric asymmetry of the magnetic field wrapping pattern in the Venusian magnetotail. *Geophysical Research Letters*, *37*, L14202. <https://doi.org/10.1029/2010GL044020>
- Zhang, T. L., Schwingenschuh, K., Russell, C. T., & Luhmann, J. G. (1991). Asymmetries in the location of the Venus and Mars bow shock. *Geophysical Research Letters*, *18*(2), 127–129. <https://doi.org/10.1029/90GL02723>